

Differential cross sections and spin density matrix elements for the reaction $\gamma p \rightarrow \phi p$

B. Dey,¹ M. Bellis,¹ C. A. Meyer,¹ and M. Williams¹

¹*Carnegie Mellon University, Pittsburgh, PA 15213*

(Dated: June 2, 2010)

High-statistics measurements of the differential cross sections and spin density matrix elements ρ_{00}^0 , ρ_{10}^0 and for the reaction $\gamma p \rightarrow \phi p$ have been made using the CLAS detector at Jefferson Lab. We cover center-of-mass energies (\sqrt{s}) from 1.97 to 2.84 GeV, with an extensive coverage in the ϕ production angle. Independent measurements were made using the charged- ($\phi \rightarrow K^+ K^-$) and neutral-mode ($\phi \rightarrow K_S^0 K_L^0$) topologies. Between $\sqrt{s} = 2$ and 2.2 GeV, there is disagreement between the charged- and neutral-mode results that suggests a ϕ - $\Lambda(1520)$ interference effect. Our extracted Pomeron slope parameter is $B_\phi \approx 3 \text{ GeV}^{-2}$ and the vector meson dominance constant is $C_\phi \approx 1.9 \mu\text{b}/\text{GeV}^2$. The ρ_{00} element is found to be large in both the Helicity and Gottfried-Jackson frames, implying helicity non-conservation in both the s - and t -channels. Consistent with previous estimates of the OZI violating deviation in the ϕ - ω mixing angle, $\Delta\theta_V \approx 3.7^\circ$, the ratio between the ϕ and ω cross sections ($R_{\phi/\omega}$) is found to be small at lower- and mid- energies. However, at the highest energies and forward-most angles, $R_{\phi/\omega}$ tends towards 1. In conjunction with the ω and pseudoscalar photoproduction results recently published by CLAS, the present data will help constrain the partial wave analyses being performed to search for missing baryon resonances.

PACS numbers: 11.80.Cr, 11.80.Et, 13.30.Eg, 14.20.Gk, 11.55.Jy

I. INTRODUCTION AND MOTIVATION

Vector meson electro- and photoproduction has played an important role in our understanding of photon-hadron interactions in QCD. Sakurai first proposed [1] that during interactions with hadrons, the photon (either real or virtual) behaves like an on shell vector meson ($V = \rho, \omega, \phi$). This is possible because the photon and the vector mesons share the same set of quantum numbers (the photon has both iso-scalar and iso-vector components). Following Feynman [2], we can write the interaction amplitude in terms of a current $J_\mu(q^2)$, as $\langle \text{hadrons} | J_\mu(q^2) | 0 \rangle$, and one sees “resonances” at the values $q^2 = m_V^2$. In this so-called vector meson dominance (VMD) model, the amplitude $\mathcal{A}_{\gamma p \rightarrow V p}$ can be directly related to $\mathcal{A}_{V p \rightarrow V p}$.

Experimentally, most of the data on vector meson photoproduction exist in the “diffractive” region of $s \rightarrow \infty, t \rightarrow 0$, where $s = (p_\gamma + p_i)^2$ and $t = (p_\gamma - p_\phi)^2$ are the squares of the total center-of-mass (*c.m.*) energy and exchanged momentum, respectively. This is the domain of perturbative QCD (pQCD). For the ϕ vector meson, even data is generally sparse [3–7] and very little data exists at either at lower energies [8–10], or at large $|t|$ [11, 12]. The CLAS Collaboration has recently published the first comprehensive measurements with high statistics and wide kinematic coverage for the $\gamma p \rightarrow \omega p$ channel [14]. In this work, we report the corresponding results for the $\gamma p \rightarrow \phi p$ channel.

In addition to the interest from the perspective of VMD phenomenology, the ϕ is also interesting because in the $SU(3)$ quark model, it appears to be an almost pure $s\bar{s}$ state while the ρ and ω mesons are made of the light u and d quarks. If we ignore the strangeness content inside the nucleons, the OZI rule implies that meson interchanges are suppressed in ϕ -nucleon interactions and the ϕ and the nucleons can only exchange

color singlet 2-gluons. The ϕ is therefore a very “clean” system to study gluonic interactions, the gluonic structure of the Pomeron, for example. There is also speculation that at near threshold and forward angles ($t \rightarrow |t|_{\min}$), the ϕ channel will give access to the 0^{++} glueball $f_0(1710)$ [15, 16].

One can also look at OZI rule violations through the ratio of the ϕ and ω differential cross-sections $R_{\phi/\omega} = \tan^2 \Delta\theta_V$, where $\theta_V \approx 35.3^\circ$ is the ϕ - ω mixing angle in $SU(3)$ [17]. Ideally, $\Delta\theta_V$ should be zero, while the current experimental estimate is $\Delta\theta_V \approx 3.7^\circ$ [17]. Such an OZI rule violation can occur either via an appreciable strangeness content inside the proton, or a large value of the coupling constant $g_{\phi NN}$. A small value for $g_{\phi NN}$ would signify suppression of N and N^* exchanges in the u -channel (backward-angles). A previous CLAS experiment [12] at $E_\gamma = 3.6 \text{ GeV}$ found that the differential cross sections showed a distinct rise at large $|t|$, pointing towards a presence of u -channel exchanges for the ϕp channel. In general, the backward angle rise is smaller than in the ωp case, but it is non-negligible. The present results confirm this as well. At high \sqrt{s} and forward-angles, $R_{\phi/\omega}$ seems to tend towards unity. This is an expected feature from the Donnachie-Landshoff (DL) model of diffractive Pomeron exchange [18]. In the DL model, the Pomeron is some kind of a gluonic object that couples to the quarks inside the hadrons as a spin-1 vector (*i.e.* $J^\mu \sim \beta_q \beta_{q'} \bar{u}_{q'} \gamma^\mu u_q$) and the coupling constant β_q is almost independent of the flavor of q .

II. EXPERIMENTAL SETUP

The data that we use in this analysis were obtained using real photons produced via bremsstrahlung from a 4.023-GeV electron beam produced by the Continuous

Electron Beam Accelerator Facility (CEBAF) at Jefferson Lab. The photons were energy tagged by measuring the momenta of the recoiling electrons with a dipole magnet and scintillator hodoscope system [13]. A separate set of scintillators was used to make accurate timing measurements. The photon energy resolution was about 0.1% of the incident beam energy and the timing resolution was 120 ps. These tagged photons were directed toward a 40-cm-long cylindrical liquid-hydrogen cryotarget inside the CEBAF Large Angle Spectrometer (CLAS) detector system, which collected data events produced by scattering. Immediately surrounding the target cell was a “start counter” scintillator, used in the event trigger.

Both the start counter and the CLAS detector were segmented into sectors with a six-fold azimuthal symmetry about the beam line. A non-uniform toroidal magnetic field with a peak strength of 1.8 T was used to bend the trajectories of charged particles and a series of drift chambers was used for charged particle tracking. In this manner, CLAS could detect charged particles and reconstruct their momenta over a large fraction of the 4π solid angle. The overall momentum resolution of the detector was $\sim 0.5\%$. A system of ~ 300 scintillators placed outside the magnetic field and drift chamber regions provided timing information by measuring the time-of-flight (TOF) for each charged particle trajectory. A fast triggering and fast data-acquisition system (capable of running at ~ 5 kHz) allowed for operating at a photon flux of a few times 10^7 photons/s. Further details of CLAS can be found in Ref. [20].

III. DATA

The specific data set that we analyze in this work was collected in the summer of 2004, during the CLAS “g11a” run period. Roughly 20 billion triggers were recorded during this time, out of which only a small fraction corresponded to ϕp events. Each event trigger required a coincidence between the photon tagger Master OR (MOR) and the CLAS Level 1 trigger. For each charged particle to trigger individually, first, a coincidence between the TOF counter scintillator hit time and the start counter hit time for that particle was required. For the Level 1 trigger to fire, two particles in two different sectors of CLAS (“two-prong” trigger) were required to trigger within a 150 ns coincidence time window. The final requirement was a coincidence between the tagger MOR and the start counter OR within a timing window of 15 ns. Also, only the first 40 tagger counters (corresponding to the higher end of the photon energy spectrum) were included in the trigger.

During offline processing, before any physics analysis began, the CLAS detector sub-systems had to be calibrated. This included determining the relative offsets between the photon tagger, start counter and TOF counter times, as well as calibration of the drift times in the drift chambers and the pulse heights of the TOF scintillators.

Energy and momentum corrections were made for individual particles to account for their energy and momentum losses during passage through several layers of the detector sub-systems. Corrections were also made to the incident photon energy (E_γ) to account for mechanical sagging in the tagger hodoscope. A detailed discussion of the collection and calibration of this data set can be found in Refs. [21, 22].

IV. REACTION TOPOLOGIES AND EVENT SELECTION

In the reaction $\gamma p \rightarrow \phi p$, the ϕ subsequently decays most of the time into two kaons. The branching fractions (*b.f.*) are 49.2% for $\phi \rightarrow K^+ K^-$ (charged-mode) and 34% for $\phi \rightarrow K_S^0 K_L^0$ (neutral-mode). For the neutral-mode, the daughter K_S^0 further decays into $\pi^+ \pi^-$ (*b.f.* 60.2%) and $\pi^0 \pi^0$ (*b.f.* 39.7%). Since CLAS was optimized for detecting charged particles, we only employ the $K_S^0 \rightarrow \pi^+ \pi^-$ decay in this analysis.

The “charged-mode” topology was then defined as $\gamma p \rightarrow K^+(K^-)p$, where only the proton and the K^+ were detected and the undetected K^- was reconstructed as the missing 4-momentum using a 1-constraint kinematic fit to a total missing mass of $m_{K^-} = 0.493$ GeV. The polarity setting of the drift chamber magnets inside CLAS bent negatively charged particles like K^- inwards toward the beam line, where the detector acceptance was the lowest. Therefore, not detecting the K^- led to a substantial increase in the overall statistics and allowed for a fine energy binning (10-MeV-wide \sqrt{s} bins) and wide kinematic coverage for this topology.

As mentioned in the introduction, it is also important to examine the neutral decay mode of the ϕ , since this is relatively immune (see discussion in Sec. ??) to effects from the $K^+ \Lambda(1520)$ channel. The “neutral-mode” topology was defined as $\gamma p \rightarrow \pi^+ \pi^- (K_L^0) p$, where only the π^+ , the π^- and proton were detected, and the undetected K_L^0 was reconstructed as the missing 4-momentum using a 1-constraint kinematic fit to $m_{K^0} = 0.497$ GeV total missing mass. The K_S^0 4-momentum was reconstructed as the sum of the π^+ and π^- 4-momenta. Since this topology required the detection of a negatively charged π^- , this topology had substantially reduced statistics compared to the charged-mode, especially at high energies and backward-angles. To bolster statistics, therefore, we employed wider 30-MeV-wide energy bins in \sqrt{s} for this case.

Each event trigger recorded by CLAS consisted of one or more tagged photons. To begin the event selection process, at least two positively charged particle tracks were required to have been detected. These were hypothesized as a proton and a K^+ for the charged-mode, and as a proton and a π^+ for the neutral-mode. The neutral-mode topology required an extra negatively charged particle track that was assumed to be a π^- . To minimize bias, all possible photon-particle combinations allowed by

Description	Topology	
	$K^+(K^-)p$	$\pi^+\pi^-(K_L^0)p$
Confidence level cut	✓	✓
Timing cuts	✓	✓
$\Lambda(1520)$ hard cut	✓	—
$M(pK)$ cut	✓	✓
K_S^0 mass cut	—	✓
Fiducial cuts	✓	✓

TABLE I: List of cuts applied to the two topologies in this analysis. The confidence level, timing and fiducial volume cuts applied to both topologies. The charged-mode analysis had an extra hard cut around $M(pK^+) \approx 1.52$ MeV to remove $K^+\Lambda(1520)$ events. The neutral-mode required an additional K_S^0 selection cut. Lastly, both topologies had a \sqrt{s} dependent cut on $M(pK)$ where the kaon was K^+ (charged-mode) or K^0 (neutral-mode).

the given topology were taken to be a candidate signal event. Events with incorrectly assigned photons or particle hypotheses were removed by subsequent cuts. In the following sub-sections, we describe each of these event selection cuts one by one, referring the interested reader to Ref. [21] for further details. Since the two topologies followed significantly different analysis chains, to avoid confusion, we list the various cuts as applicable to each of the charged- and neutral-mode topologies in Table I.

A. Confidence level cut

Each event in the charged-mode data set was kinematically fit to an overall m_{K^-} missing mass hypothesis for the undetected K^- . For every event recorded by CLAS, both “ $K^+ : p$ ” and “ $p : K^+$ ” combinations were treated as independent event hypotheses, where the two particle assignments (separated by the colon) corresponded to the two detected positively charged particles. Similarly, for the neutral-mode, every event was kinematically fit to an overall m_{K^0} missing mass hypothesis for the undetected K_L^0 . Both “ $\pi^+ : p : \pi^-$ ” and “ $p : \pi^+ : \pi^-$ ” combinations, corresponding to different particle assignments to the two positively charged tracks, were taken as independent event hypotheses.

The kinematic fitter adjusted the momenta of each individual detected particle, while constraining the total missing mass to be either m_{K^-} (charged-mode) or m_{K^0} (neutral-mode). The shifts in the momenta, combined with the known detector resolution within the current experiment, gave a confidence level for the event to be the desired reaction. For a properly tuned kinematic fitter, background events have low confidence levels, while real signal events populate the confidence level with a flat distribution. The confidence level distribution for the charged-mode topology is shown in Fig. 1. The peak near zero came from background events, and above $\sim 15\%$, the distribution was fairly flat, as expected for real signal events. The neutral-mode topology confidence level

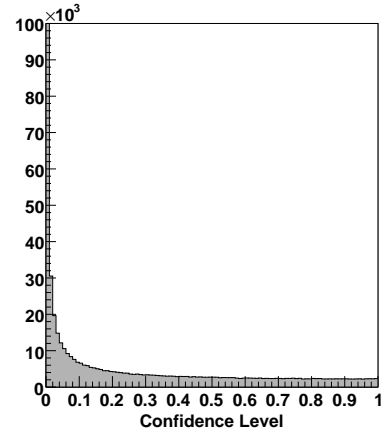


FIG. 1: (Color On-line) Confidence levels from a kinematic fit to $\gamma p \rightarrow K^+(K^-)p$ for the charged-mode topology. Background events mostly occupied the region about zero. These were removed by placing a 10% cut on the confidence level. Above $\sim 15\%$ or so, the distribution was fairly flat, as expected for real signal events. The neutral-mode confidence level also had very similar features.

distribution had similar features as well. For both topologies, only events with a confidence level greater than 10% were retained for further analysis.

B. Timing cuts

Track reconstruction through the different CLAS detector segments yielded both the momentum \vec{p} and the path length l from the reaction vertex to the TOF scintillator wall. The expected time-of-flight for a track hypothesized to be a particle of mass m was then given by

$$t_{exp} = \frac{l}{c} \sqrt{1 + \left(\frac{m}{p}\right)^2}. \quad (1)$$

CLAS also measured the time-of-flight t_{meas} as the difference between the tagged photon's projected arrival time at the reaction vertex for the given event and the time the given particle track hits the TOF scintillator wall. The difference between these two time-of-flight calculations gave $\Delta tof = t_{meas} - t_{exp}$. For each track there was also a calculated mass m_c , given by

$$m_c = \sqrt{\frac{p^2(1 - \beta^2)}{\beta^2 c^2}}, \quad (2)$$

where $\beta = l/(ct_{meas})$.

Timing information in the form of Δtof or m_c was used to place particle identification cuts on the proton and K^+ tracks for the charged-mode, and the proton

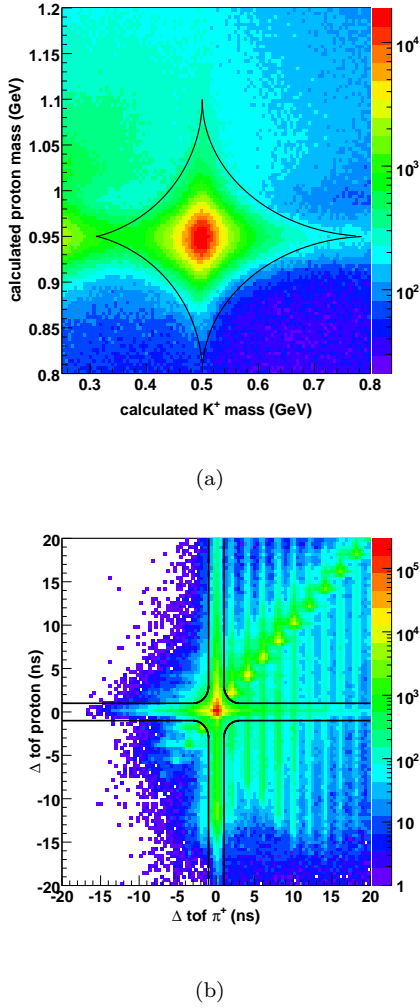


FIG. 2: (Color On-line) Timing cuts for background removal: (a) charged-mode topology, (b) neutral-mode topology. Events lying outside the quadrant of black curves in both figures were removed from further analysis. Note the logarithmic scale for the intensity axes.

and π^+ tracks for the neutral-mode. As mentioned earlier, for each pair of positively charged particle tracks, all possible combinations of particle assignments were considered and treated as independent event hypotheses. The cuts are shown in Fig. 2, where events outside the quadruplet of black curves were rejected. The clusters along the diagonal in Fig. 2b, were due to accidental coincidences with events in different beam bursts corresponding to the 2 ns radio-frequency pulses used by the CEBAF electron accelerator.

C. $\Lambda(1520)$ removal cut

Consider the process $\gamma p \rightarrow M(\sqrt{s}) \rightarrow K^+ K^- p$ from the perspective of a 3-body reaction, where $M(\sqrt{s})$ de-

notes a general s -channel state with total invariant mass \sqrt{s} . If $M(K^+ K^-)$ is fixed at $m_\phi \approx 1.02$ GeV, $M(pK^-)$ is bound between a minimum ($M_{pK,min}$) and a maximum ($M_{pK,max}$) corresponding to the proton and K^- directions being parallel or anti-parallel, respectively. The specific values of $M_{pK,min}$ and $M_{pK,max}$ depend on \sqrt{s} , and the masses of the ϕ , the proton and the kaon. Fig. 3a shows the variation of $M_{pK,min}$ and $M_{pK,max}$ with \sqrt{s} . In the region $2 \text{ GeV} \leq \sqrt{s} \leq 2.2 \text{ GeV}$, $M(pK^-) = 1.52 \text{ GeV}$ lies within these bounds. This implies that in this energy regime, the kinematics for the reactions ϕp and $K^+ \Lambda(1520)$ overlap in phase-space. Figs. 3b and 3c shows Dalitz plots of $M(pK^-)$ vs. $M(K^+ K^-)$ at two different energies. The ϕ and $\Lambda(1520)$ “bands” are clearly visible in both figures. Above $\sqrt{s} \approx 2.2 \text{ GeV}$ there is no overlap between the ϕ and the $\Lambda(1520)$.

In this analysis we have applied two types of cuts to reduce the $\Lambda(1520)$ contamination. Firstly, we apply a \sqrt{s} dependent cut

$$M_{pK,min}(\sqrt{s}) \leq M(pK^-) \leq M_{pK,max}(\sqrt{s}) \quad (3)$$

that effectively removes the $\Lambda(1520)$ background above $\sqrt{s} \approx 2.2 \text{ GeV}$, since $M(pK^-) = 1.52 \text{ GeV}$ falls outside the $M_{pK,min}(\sqrt{s})$ and $M_{pK,max}(\sqrt{s})$ bounds in this energy region. However, in the overlap region between $\sqrt{s} = 2$ and 2.2 GeV , this cut will not be able to remove the $\Lambda(1520)$ events leaking in, because here, $M(pK^-) = 1.52 \text{ GeV}$ falls within the $M_{pK,min}(\sqrt{s})$ and $M_{pK,max}(\sqrt{s})$ limits. The only way to remove the $\Lambda(1520)$ background is through our signal-background separation procedure, described in Sec. ???. In keeping with this feature in the ϕ - $\Lambda(1520)$ overlap region, we keep the additional option of placing a hard cut around the $\Lambda(1520)$ mass as

$$|M(pK^-) - 1.52| \geq \delta, \quad (4)$$

where the trial values for δ were taken as 5, 10 and 15 MeV. Further details on the necessity and application of this hard cut is given in Sec. ??.

D. General $M(pK)$ cut

The above argument of an energy dependent bound for $M(pK)$ can be extended to the neutral-mode topology as well, with K^- in Eq. 3 replaced by either K_S^0 or K_L^0 . Fig. [?] shows the effect of this cut on the neutral-mode topology. The dashed histogram in blue represents the set of rejected events and the shaded histogram represents the events passing the cut.

E. K_S^0 selection cut

In the neutral-mode topology, the K_S^0 is not detected directly, but reconstructed as the sum of the π^+ and π^-

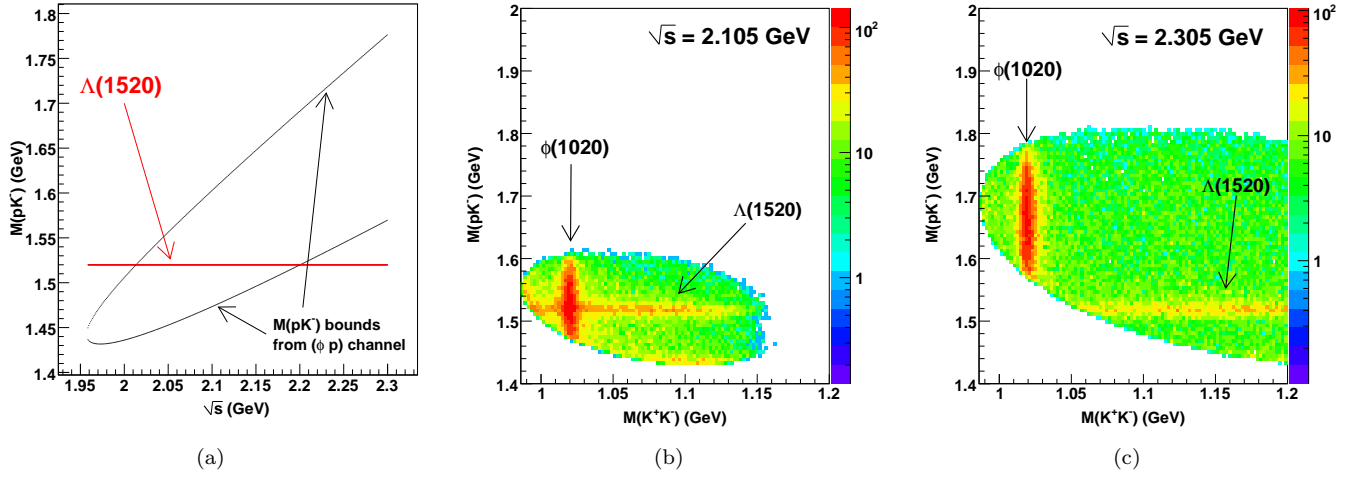


FIG. 3: (Color On-line) ϕ - $\Lambda(1520)$ overlap for the charged-mode topology: (a) if the $M(K^+K^-)$ invariant mass is fixed at $m_\phi = 1.020$ GeV, $M(pK^-)$ is bound between an upper and lower limit depending on \sqrt{s} . Between $\sqrt{s} = 2$ and 2.2 GeV, the $\Lambda(1520)$ mass lies within these bounds and the ϕp and $K^+\Lambda(1520)$ channels overlap in phase-space. A Dalitz plot of $M(pK^-)$ vs. $M(K^+K^-)$ is shown in (b) and (c) for two different energies. (b) Shows the overlap for the $\sqrt{s} = 2.105$ GeV bin, while (c) shows that above $\sqrt{s} \approx 2.2$ GeV, the ϕ and $\Lambda(1520)$ “bands” are separated.

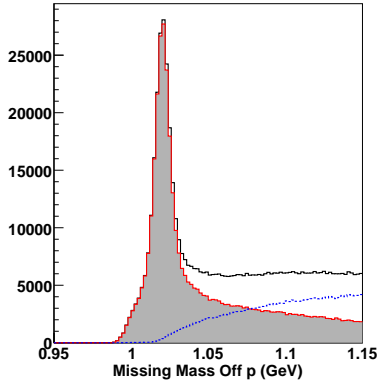


FIG. 4: (Color On-line) Effect of the \sqrt{s} dependent cut on $M(pK)$ employing Eq. 3 (with K^- replaced by K_S^0 or K_L^0), for the neutral-mode topology. The dashed histogram in blue are the rejected events and the shaded histogram represents the events that passed the cut.

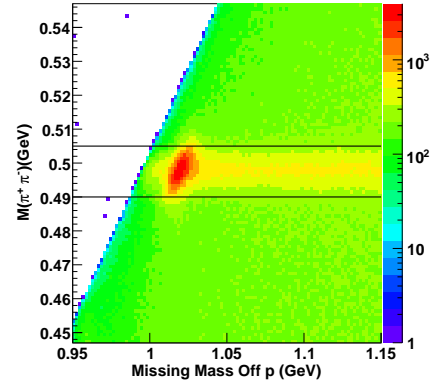


FIG. 5: (Color On-line) The reconstructed K_S^0 mass plotted vs. the ϕ mass for the neutral-mode. The cut boundaries are shown by the two horizontal lines.

momenta. To select the K_S^0 , we applied a cut around the m_{K^0} (≈ 0.497 GeV) mass as

$$0.49 \text{ GeV} \leq M(\pi^+\pi^-) \leq 0.505 \text{ GeV}. \quad (5)$$

Fig. 5 shows $M(\pi^+\pi^-)$ plotted against the reconstructed ϕ mass. The cut boundaries are shown by the two horizontal lines in bold.

F. Effectiveness of cuts

The effectiveness of these cuts can be gauged by the percentage of “signal” events lost due to them. The $MM(K^+)$ distributions were fit to a Gaussian signal plus a quartic background function before and after placing the cuts. From this study, the loss in signal yields due to the cuts was estimated to be $\sim 1.8\%$ for the two-track and $\sim 0.62\%$ for the three-track topologies [21]. We quote these as the upper limits of the systematic uncertainties in our particle identification/event selection for this analysis.

G. Fiducial cuts

In addition to the above particle identification cuts, fiducial volume cuts were required to remove events belonging to regions where our understanding of the detector performance was relatively poor. These cuts were motivated by differences in an empirical efficiency calculation between the actual data and Monte Carlo which indicated discrepancies in the forward-angle region and at the boundaries of the six sectors of the CLAS detector due to edge effects in the drift chambers. Therefore, events with any particle trajectory falling near the sector boundary regions were removed. A ϕ_{lab} -dependent cut on $\cos\theta_{lab}$ along with a hard cut at $\cos\theta_{lab} \geq 0.985$ removed extremely forward-going particles that coincided with the beam-dump direction. Localized inefficiencies within the CLAS detector volume such as inside the drift chambers were accounted for by placing trigger efficiency cuts on the Monte Carlo data as functions of ϕ_{lab} , θ_{lab} and $|\vec{p}|$ for each particle track. Additional cuts were placed on backward-going tracks ($\cos\theta_{lab} \leq -0.5$). A minimum proton momentum cut at 375 MeV removed slow moving protons, whose energy losses were difficult to model in the detector simulation. Events with particles corresponding to poorly performing TOF scintillator counters were removed as well.

V. SIGNAL BACKGROUND SEPARATION

The event selection cuts were very effective in cleaning the data sample for both topologies. Further removal of background, non- ϕn events, was affected by an event-based technique that sought to preserve correlations between all independent kinematic variables [21, 23]. The motivation behind this approach, as opposed to a more conventional sideband-subtraction method, was as follows.

For a reaction with multiple decays, such as in the present case, there are several independent kinematic variables (decay angles, for instance). To perform a background subtraction, one typically bins the data in a particular variable, such as the production angle $\theta_{c.m.}^\phi$. This is because the background level can vary widely within the range of the kinematic variable chosen. However, this binning in a single variable generally does *not* preserve correlations present in the other independent kinematic variables of interest. Therefore, one needs to bin the data in multiple kinematic variables, such that in any particular bin, the background level (both shape and size) remains roughly the same. Finally, the event-based fits using partial wave amplitudes that we employ in the Monte Carlo to calculate the acceptance for the three-track topology (see Sec. VI) are specifically intended to reproduce the correlations present in the data. Thus, the need for a more sophisticated background separation approach.

To execute this technique for a given event, first, an

N_c number of “closest neighbor” events were chosen in the phase space of all independent kinematic variables. N_c was typically of the order of a hundred. These $N_c + 1$ events were then fitted to a signal function $s(m)$ plus a background function $b(m)$ using an event-based, unbinned, maximum likelihood method (the fit variable m being $MM(p)$). Once the functions $s_i(m)$ and $b_i(m)$ had been obtained from this fit for the i^{th} event, the event was assigned a signal quality factor Q_i given by:

$$Q_i = s_i(m_i) / (s_i(m_i) + b_i(m_i)). \quad (6)$$

The Q -factor was then used to weigh the event’s contribution for all subsequent calculations. In particular, the signal yield in a kinematic bin with N events was obtained as

$$\mathcal{Y} = \sum_i^N Q_i. \quad (7)$$

For yield extraction, previous experiments used a Gaussian function to represent the ϕ signal. In this analysis, we have used an unsymmetric Breit-Wigner to better characterize the ϕ lineshape. This is more appropriate because the ϕ mean mass $m_0 \approx 1.019$ GeV is close to the $2K$ threshold (≈ 0.99 GeV). The $\phi \rightarrow KK$ decay is an $L = 1$ P -wave decay. In the ϕ rest frame, the maximum orbital angular momentum L of the KK system is limited by the break-up momentum $q(m) = \sqrt{m^2 - m_K^2}/2$ for a ϕ mass m . The daughter K particles moving slowly with an impact parameter (meson radius) d of the order of 1 fm ($d = 0.1973$ GeV) have difficulty in generating sufficient L to conserve the overall angular momentum. Therefore, each angular momentum amplitude has to be weighted by the barrier factor given by the Blatt-Weisskopf function B_L [?]. For $L = 1$, $B_L = \sqrt{2z/(1+z^2)}$, where $z = q/d$. The mass dependent Breit-Wigner width is then given by

$$\Gamma(m) = \Gamma_0 \left(\frac{q}{q_0} \right)^{2L+1} \left(\frac{m_0}{m} \right) \left(\frac{B_0}{B} \right), \quad (8)$$

where the subscript 0 denotes evaluation at the ϕ mean mass $m_0 = 1.019$ GeV, and $\Gamma_0 = 4$ MeV. The overall signal function was a Voigtian function, *i.e.*, the convolution of non-relativistic Breit-Wigner (with a mass-dependent width, explained above) and a Gaussian function for the detector resolution.

Calculations were repeated using different forms of the background function and several different values of N_c , without any noticeable systematic shifts in the yields. The trial background functions were a general quartic, and an empirical function used in a previous CLAS experiment [?] of the form $f(m) = A\sqrt{m^2 - (2m_K)^2} + B(m^2 - (2m_K)^2)$ to represent the KK phase space background above the threshold mass $2m_K \approx 0.99$ GeV. The values of N_c were taken as 50, 100, 150, 200 and 300. As long as N_c was greater than ≈ 50 , the fits were stable. The final results presented here used a quartic background and $N_c = 200$.

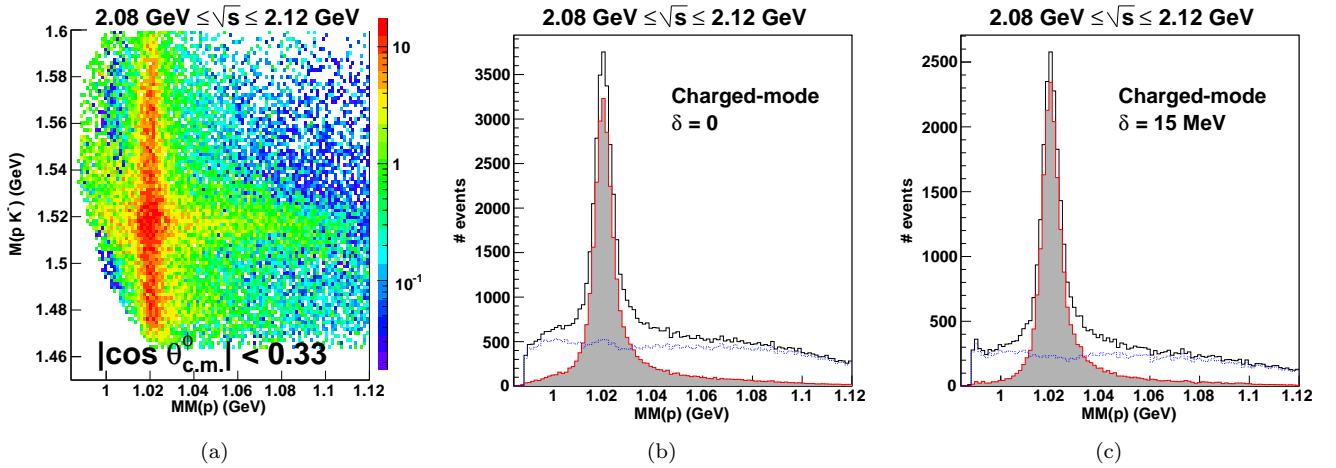


FIG. 6: (Color On-line) Signal background separation for the charged-mode topology in the ϕ - $\Lambda(1520)$ overlap region. (a) Shows a plot of $M(pK^-)$ vs. $MM(p)$ for the mid-angle region ($|\cos \theta_{c.m.}^\phi| < 0.33$) after all cuts and background separation. The distinct “band” around $M(pK^-) \approx 1.52$ GeV shows the remnant $\Lambda(1520)$ background. This feature was also present in the more backward- and forward-angles, but to a less pronounced degree. The ϕ mass distribution is shown in (b). In figures (b) and (c), the red (shaded) histograms are the data weighted by Q , representing the signal, while the blue (dotted) histograms are the data weighted by $(1 - Q)$, representing the background. The effect of the hard cut $|M(pK^-) - 1.52| < \delta$ is shown with (b) $\delta = 0$ and (c) $\delta = 15$ MeV.

For the charged-mode topology, fits were initially run without employing the hard-cut around the $\Lambda(1520)$ mass given by Eq. 4. We found that in the ϕ - $\Lambda(1520)$ overlap region (\sqrt{s} between 2 and 2.2 GeV), our background separation method was not able to fully remove the $K^+\Lambda(1520)$ background. The contribution of the remnant $K^+\Lambda(1520)$ background was also found to have an angular dependence, being most pronounced in the mid-angle regions. Fig. 6a shows a plot of $M(pK^-)$ vs. $MM(p)$ for \sqrt{s} between 2.08 GeV and 2.12 GeV and $|\cos \theta_{c.m.}^\phi| < 0.33$ (mid-angles) after signal-background subtraction. That is, every event has been weighted by its corresponding Q value. The “band” around $M(pK^-) = 1.52$ GeV is distinctly visible. This effect was less pronounced in either the more forward- or the more backward-angle regions.

In keeping with these observations we decided to employ the hard cut around $M(pK^-)$ as given by Eq. 4. Three values of the cut width, $\delta = 5, 10$ and 15 MeV were tried out. Our final results used $\delta = 15$ MeV. By choosing such a stringent value of the width δ , we intend to gauge the maximal effect of the ϕ - $\Lambda(1520)$ overlap in our differential cross section and spin density matrix elements. We will present results both with and without the use of the hard cut. The comparison between $\delta = 0$ and $\delta = 15$ MeV should facilitate future studies of this effect. For Figs. 6b and 6c, the shaded histograms represent the extracted signal where each event has been weighted by its corresponding Q value. The blue histograms represent the background with each event weighted by $(1 - Q)$. Fig. 6b shows with case without the application of the hard cut, while Fig. 6c includes a $\delta = 15$ MeV cut around

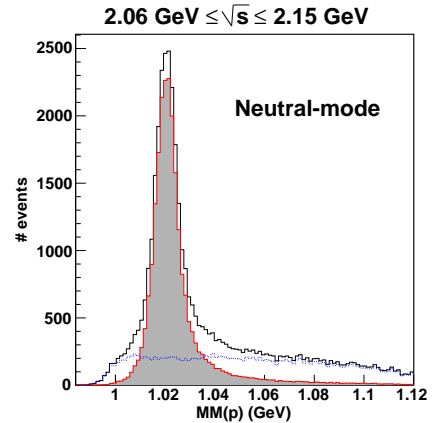


FIG. 7: (Color On-line) Signal background separation for the neutral-mode topology. The red (shaded) and blue (dotted) histograms represent the signal (each event weighted by Q) and the background (weighted by $(1 - Q)$), respectively.

$M(pK^-) = 1.52$ GeV. Our estimated total signal yields are ~ 0.477 million for $\delta = 0$ (without the $\Lambda(1520)$ hard cut) and ~ 0.436 million for $\delta = 15$ MeV (with the hard cut). Note that above $\sqrt{s} \approx 2.2$ GeV, the $\Lambda(1520)$ cut plays no role.

Fig. 7 shows the method as applied to the neutral-mode topology. Our \sqrt{s} bins are 30-MeV wide, and Fig. 7 shows the total yields over three energy bins (\sqrt{s} from 2.06 GeV to 2.15 GeV). We remind the reader that the ϕ - $\Lambda(1520)$ overlap plays no role here, since the fi-

nal state particles are different for the ϕ neutral-mode and the $\Lambda(1520)$. Our estimated total signal yield for this topology after all cuts and background separation is ~ 0.097 million, *i.e.* around a fifth of the charged-mode topology.

VI. DETECTOR ACCEPTANCE

Detector efficiency was modeled using GSIM, a GEANT-based simulation package of the CLAS detector. 100 million $\gamma p \rightarrow \phi p$ events were pseudo-randomly generated according to phase-space distributions and allowed to propagate through the simulation. The simulator also handled the decay of the ϕ into the KK charged- and neutral-modes according to the corresponding branching fractions. An additional momentum smearing algorithm was applied to better match the resolution of the Monte Carlo with the real data. After processing, the “raw” (*i.e.*, original phase space generated) events yielded a set of “accepted” Monte Carlo events. The “accepted” Monte Carlo data then underwent the exact same series of event reconstruction, analysis cuts and energy-momentum correction steps as applied to the real data events.

To account for the characteristics of the event trigger used in this experiment, two additional corrections went into the accepted Monte Carlo. The first of these corrections came from a trigger efficiency study using the $\gamma p \rightarrow p\pi^+\pi^-$ channel. This study computed the probability that an individual particle trajectory did *not* fire the trigger, when the reaction kinematics strongly demanded (via total missing mass) that the particle should have been there. The average effect of this correction was found to be 5-6%.

To form a more accurate characterization of the detector acceptance pertaining to the kinematics of the reaction of interest, one should use a Monte Carlo event generator based on a physics model, instead of a simple phase-space generator. Typically, this is achieved in an iterative fashion; one starts with phase-space generated Monte Carlo events, extracts the differential cross sections, fits these cross sections to a model and uses the model to generate new Monte Carlo events for the next iteration. After several such iterations, the accepted Monte Carlo and data distributions are expected to resemble each other to a fair degree.

However, the above procedure assumes that one has a very good handle on the signal-background separation. For a complicated reaction with multiple decay angles, the detector acceptance can depend on several kinematic variables and it becomes more difficult to disentangle the effect of the detector acceptance on signal events from that on the background. Our signal-background separation procedure, as described in the previous section, specifically addresses this issue. By weighting every event by its Q -value, we are able to produce distributions of any particular kinematic variable that include only sig-

nal events.

In the next step, we expand the scattering amplitude \mathcal{M} for each of the complete reaction chains $\gamma p \rightarrow \phi p \rightarrow K^+K^-p$ (charged-mode) and $\gamma p \rightarrow \phi p \rightarrow K_S^0 K_L^0 p \rightarrow \pi^+\pi^- K_L^0 p$ (neutral-mode) in a basis of s -channel production amplitudes

$$\mathcal{M}_{\vec{m}}(\vec{x}, \vec{\alpha}) \approx \sum_{J=\frac{1}{2}}^{\frac{11}{2}} \sum_{P=\pm} A_{\vec{m}}^{JP}(\vec{x}, \vec{\alpha}), \quad (9)$$

where $\vec{m} = \{m_\gamma, m_i, m_\phi, m_f\}$ denotes spin projections quantized along the beam direction for the incident photon, target proton, intermediate ϕ and final-state proton, respectively. The vector \vec{x} represents the set of kinematic variables that completely describes the reaction, while the vector $\vec{\alpha}$ denotes a set of 56 fit parameters, estimated by a fit to the data distribution using the method of unbinned maximum likelihoods. The only assumption made here is that any distribution can be expanded in terms of partial waves (denoted by the spin-parity combination J^P). Ideally, one needs to use a “complete” basis of such J^P waves, but we found that a “large-enough” ($J^P = \frac{1}{2}^\pm, \frac{3}{2}^\pm, \dots, \frac{11}{2}^\pm$) set of waves was sufficient to fit the data very well. The s -channel J^P waves were constructed using the relativistic Rarita-Schwinger formalism [24] and numerically evaluated using the `qft++` software package [25]. A full description of the amplitude construction and fitting procedure can be found in Ref. [21].

Based on these fit results, each accepted Monte Carlo event was assigned a weight I_i given by,

$$I_i = \sum_{m_\gamma, m_i, m_f, m_{\gamma f}} \left| \sum_{m_\Sigma} \mathcal{M}_{\vec{m}}(\vec{x}_i, \vec{\alpha}) \right|^2, \quad (10)$$

where we have coherently summed over the intermediate ϕ spins. The accepted Monte Carlo weighted by the fits matched the data in all physically significant distributions and correlations, as shown in Fig. ?? for the production angle. The detector acceptance as a function of the kinematic variables \vec{x} was then calculated as

$$\eta_{wtd}(\vec{x}) = \left(\sum_i^{N_{acc}} I_i \right) / \left(\sum_j^{N_{raw}} I_j \right), \quad (11)$$

where N_{raw} and N_{acc} denote the number of events in the given kinematic bin for the raw and the accepted Monte Carlo data sets, respectively.

VII. NORMALIZATION

To calculate differential cross sections, the data yields were normalized by the photon flux and the target factors

as

$$\frac{d\sigma}{d\cos\theta_{c.m.}^\phi}(\sqrt{s}, \cos\theta_{c.m.}^\phi) = \left(\frac{A_t}{\mathcal{F}(\sqrt{s})\rho_t\ell_t N_A} \right) \times \frac{\mathcal{Y}(\sqrt{s}, \theta_{c.m.}^\phi)}{(\Delta\cos\theta_{c.m.}^\phi)\eta(\sqrt{s}, \cos\theta_{c.m.}^{K^+})}, \quad (12)$$

where A_t , ρ_t , and ℓ_t were the target atomic weight, density and length, respectively, N_A was the Avogadro constant, $\mathcal{F}(\sqrt{s})$ was the photon flux incident on the target for the given \sqrt{s} bin, $\Delta\cos\theta_{c.m.}^\phi$ was the angular binning width, and $\mathcal{Y}(\sqrt{s}, \cos\theta_{c.m.}^\phi)$ and $\eta(\sqrt{s}, \cos\theta_{c.m.}^{K^+})$ were the number of data events and the acceptance for the given kinematic bin, respectively.

Photon flux normalization for this analysis was carried out by measuring the rate of out-of-time electrons at the photon tagger, that is, hits that did not coincide with any event recorded by CLAS. Corrections were made to account for photon losses along the beam line and the detector dead-time.

A separate correction to the photon flux normalization was required to account for the fact that only the first two-thirds of the photon tagger counters (1-40) went into the trigger. “Accidental” events corresponding to tagger counters 41-61 could trigger if a simultaneous hit occurred in the lower (1-40) counters within the same time window. Such “accidental” events would be triggered as usual and recorded by CLAS just as any other “normal” event. However, the photon flux calculation would not incorporate the associated photon corresponding to an invalid tagger counter. By utilizing the trigger rates in counters 1-40 and assuming a Poisson distribution for the probability of occurrence of such “accidental” events, we were able to correct for this feature. Faulty tagger electronics prevented accurate electron rate measurements for photons in the energy bins $\sqrt{s} = 2.735$ and 2.745 GeV [21]. Differential cross sections are therefore not reported at these three energies. However, polarization measurements do not depend on flux normalizations and are reported in these three bins.

VIII. UNCERTAINTIES

The statistical uncertainties for the differential cross sections were comprised of the uncertainty in the data yield and the acceptance calculation. For the i^{th} event, the covariance matrix from the signal-background fit described in Sec.?? gave the uncertainty σ_{Q_i} in our estimate of the signal quality factor Q_i . Summing up these uncertainties, assuming 100% correlation for events in a given $(\sqrt{s}, \cos\theta_{c.m.}^\phi)$ bin, the statistical uncertainty in the data yield was given by

$$\sigma_{data}^2 = \mathcal{Y} + \left(\sum_i^{N_{data}} \sigma_{Q_i} \right)^2. \quad (13)$$

Source of Uncertainty	Topology	
	$K^+p\pi^-(\gamma)$	$K^+p(\pi^-, \gamma)$
Particle ID	0.62%	1.8%
Kinematic Fitter	3%	—
Detector Acceptance	4%-6%	4%-6%
Flux Normalization	7.7%	7.7%
Detector Live-time	3%	3%
Transmission efficiency	0.5%	0.5%
Target Characteristics	0.2%	0.2%
$\Lambda \rightarrow p\pi^-$ Branching Fraction	0.5%	0.5%
Overall estimate	9.7%-10.7%	9.4%-10.4%

TABLE II: List of systematic uncertainties for this analysis. The three-track topology has a lower PID uncertainty than the two-track topology but acquires an additional uncertainty from the kinematic fitting systematics.

The relative statistical uncertainty in the acceptance calculation was computed using the expression [26]

$$\delta\eta/\eta = \sqrt{\frac{1/\eta - 1}{N_{raw}}}. \quad (14)$$

Given the overall azimuthal symmetry of the detector about the beam direction, the data yields in each of the six sectors in the CLAS detector (as tagged by the sector in which the K^+ belongs) should have been statistically comparable after acceptance corrections. By examining deviations from this symmetry, we estimated the relative systematic uncertainty in our acceptance calculation to be between 4 to 6%, depending on \sqrt{s} . Data collection for the present experiment occurred in bunches of about 10 million event triggers (called “runs”). Our estimated photon flux normalization uncertainty from a “run”-wise comparison of the flux-normalized ϕp yields was 3.2% [21].

In photoproduction experiments, overall normalization uncertainties are often estimated by comparing the total πN cross sections with other world data. Since the event trigger for the current experiment required detection of at least *two* charged tracks, the πN channel was not available here. However, a careful study of the cross sections for three different reactions (ωp , $K^+\Lambda$ and ηp) using the same (present) data set in comparison with other experiments gave a flux normalization uncertainty of 7%. Combining this in quadrature with the uncertainty in the run-by-run flux-normalized yield and contributions from photon transmission efficiency (0.5%), live-time (3%) and target density and length (0.2%), we quote an overall normalization uncertainty of 8.3%. The last contribution comes from the $\Lambda \rightarrow p\pi^-$ branching fraction (0.5%). A list of all the systematic uncertainties pertaining to $d\sigma/d\cos\theta_{c.m.}^{K^+}$ measurements for each of the two topologies is given in Table II.

IX. SPIN DENSITY MATRIX ELEMENTS

A massive vector boson like the ϕ meson has three physical spin components. These three spin operators are

$$S_x = \frac{1}{\sqrt{2}} \begin{pmatrix} 0 & 1 & 0 \\ 1 & 0 & 1 \\ 0 & 1 & 0 \end{pmatrix}, \quad (15a)$$

$$S_y = \frac{1}{\sqrt{2}} \begin{pmatrix} 0 & -i & 0 \\ i & 0 & -i \\ 0 & i & 0 \end{pmatrix}, \text{ and} \quad (15b)$$

$$S_z = \begin{pmatrix} 1 & 0 & 0 \\ 0 & 0 & 0 \\ 0 & 0 & -1 \end{pmatrix}, \quad (15c)$$

and any pure spin-polarization state $|\alpha\rangle$ can be expanded in terms of the eigenstates of S_x , S_y and S_z . A classical ensemble of states is given as $|\psi\rangle = \sum_{\alpha} w_{\alpha} |\alpha\rangle$, with the normalization $\sum_{\alpha} w_{\alpha} = 1$. For more general states that are not classical ensembles, the description is given in terms of a density matrix ρ . This is a 3×3 Hermitian matrix with unit trace. The Hermiticity property reduces the number of real independent variables to 9 (3 complex off-diagonal and 3 real diagonal elements) while the trace condition further reduces this number by 1. Therefore, 8 spin operators are needed to form a complete basis for expanding any vector meson density operator. Three of these are the vector operators \vec{S} and the rest are given by the 5 rank-2 tensor operators τ_{ij} as

$$\tau_{ij} = \frac{3}{2} (S_i S_j + S_j S_i) - 2\delta_{ij}. \quad (16)$$

In the tensorial space indexed by the two rank-1 tensors S_i and S_j , τ_{ij} is symmetric and traceless.

The above tensors were written in the Cartesian basis. Following Ref. [27], we switch to the helicity basis where the spin-1 operators are written as [28]

$$S_{1\pm 1} = \mp \frac{S_x \pm iS_y}{\sqrt{2}}, \quad S_{10} = S_z. \quad (17)$$

In the helicity basis, the rank-2 operators $\tau_{2\mu}$ are given by the tensor products $[S_1 \otimes S_1]_{\mu}$, $\mu = \{0, \pm 1, \pm 2\}$. Substituting the appropriate Clebsch-Gordan coefficients, the tensor polarization operators are

$$\tau_{22} = S_{11}S_{11} \quad (18a)$$

$$\tau_{2-2} = S_{1-1}S_{1-1} \quad (18b)$$

$$\tau_{21} = \frac{1}{\sqrt{2}} (S_{11}S_{10} + S_{10}S_{11}) \quad (18c)$$

$$\tau_{2-1} = \frac{1}{\sqrt{2}} (S_{1-1}S_{10} + S_{10}S_{1-1}), \text{ and} \quad (18d)$$

$$\tau_{20} = \frac{1}{\sqrt{6}} (S_{11}S_{1-1} + 4S_{10}S_{10} + S_{1-1}S_{11}). \quad (18e)$$

The full expression of the density matrix is then given as

$$\rho = \frac{1}{3} \left[I + \frac{3}{2} \vec{S} \cdot \vec{P} + \sqrt{3} \tau \cdot T \right], \quad (19)$$

with the vector polarizations defined as

$$P_{1\pm 1} = \mp \frac{P_x \pm iP_y}{\sqrt{2}}, \quad P_{10} = P_z, \quad (20)$$

and the sum over the tensor polarizations defined as

$$\tau \cdot T = \sum_{\mu=0, \pm 1, \pm 2} (-1)^{\mu} \tau_{2-\mu} T_{2\mu}. \quad (21)$$

For unpolarized beam and target polarizations, parity conservation leads to the condition $\rho_{\lambda\lambda'} = (-1)^{\lambda-\lambda'} \rho_{-\lambda-\lambda'}$. Along with the hermiticity property $\rho_{\lambda\lambda'} = \rho_{\lambda'\lambda}^*$, this implies [27] $P_x = P_z = 0$, T_{20} , T_{21} and T_{22} be real, $T_{2-1} = -T_{21}$, and $T_{2-2} = T_{22}$. The most general form density matrix for unpolarized photo-production is given as (following the sign conventions in Ref. [29])

$$\rho = \begin{pmatrix} \frac{1-\rho_{00}}{2} & \rho_{10} & \rho_{1-1} \\ \rho_{10}^* & \rho_{00} & -\rho_{10}^* \\ \rho_{1-1} & -\rho_{10} & \frac{1-\rho_{00}}{2} \end{pmatrix}, \quad (22)$$

where ρ_{00} and ρ_{1-1} are purely real and only ρ_{10} has both real and imaginary parts. The physical interpretation of the spin density matrix elements (SDME) are [27] $P_y = -2\sqrt{2} \text{Im} \rho_{10}$, $T_{20} = \frac{1}{2}(1 - 2\rho_{00})$, $T_{21} = -\sqrt{6} \text{Re} \rho_{10}$ and $T_{22} = \sqrt{3} \rho_{1-1}$.

Even though the density matrix given by Eq. 22 consists of four real independent observables, for the vector meson decaying into pseudoscalar mesons ($\phi \rightarrow KK$, $\rho \rightarrow \pi\pi$ or $\omega \rightarrow \pi\pi\pi$), there are only three measurable quantities. For these decays, the intensity distribution is given by the Schilling's equation [29]

$$\mathcal{I} \sim \frac{1}{2}(1 - \rho_{00}) + \frac{1}{2}(3\rho_{00} - 1) \cos^2 \zeta - \sqrt{2} \text{Re} \rho_{10} \sin 2\zeta \cos \varphi - \rho_{1-1} \cos 2\varphi, \quad (23)$$

where ζ and φ are the polar and azimuthal angles of the vector meson decay into pseudoscalar mesons. Since Eq. 23 does not include $\text{Im} \rho_{10}$, therefore P_y is not measurable. Since P_x and P_z are also constrained to be 0 for unpolarized beam-target configurations, the vector polarization \vec{P} is not measurable at all. Kloet *et al.* ?? has shown that the only way to measure the vector polarization is through leptonic decays of the vector mesons, with the additional requirement that one of the lepton spins be also measured.

A. Helicity conservation and choice of reference frames

The choice of the reference frame for the two decay angles in the intensity distribution of Eq. 23 depends on the

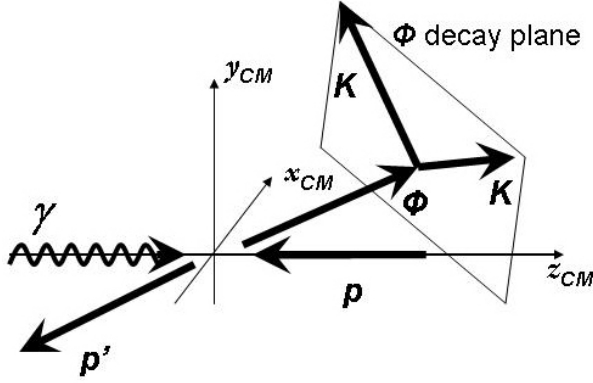


FIG. 8: A schematic diagram of the reaction chain $\gamma p \rightarrow \phi p' \rightarrow KKp'$ in the overall center-of-mass frame. The beam direction is taken as the positive z -axis, and the y -axis is normal to the ϕ production plane.

production mechanism under examination. Three prevalent choices exist in the literature, the Adair frame, the Helicity frame, and the Gottfried-Jackson frame. In the Adair (Ad) frame, the polarization axes from both the incoming and outgoing states are chosen as the z -axis (along the beam direction). The Adair frame is convenient when the production mechanism conserves spin in the s -channel $c.m.$ frame. For the Helicity (Hel) frame, the vector meson direction in the $c.m.$ system defines the quantization axis. This is preferred for s -channel helicity conservation (SCHC). Under the assumptions of SCHC, $\rho_{00}^{Hel} = \rho_{10}^{Hel} = \rho_{1-1}^{Hel} = 0$ [30]. For the Gottfried-Jackson (GJ) frame, one makes a further boost to the vector meson rest-frame from the overall $c.m.$ frame. The quantization axis is along the direction of the incoming photon, as seen in the vector meson rest-frame. For a t -channel exchange of X , the momentum of the incoming photon and X is collinear in the GJ frame. Therefore the ρ elements measure the degree of helicity flip due to the t -channel exchange of X in the GJ frame. For example, if the t -channel exchange particle is a $J^P = 0^+$ state, then no helicity flip will occur (TCHC) and the vector meson will have the same helicity as the incoming photon. For this case $\rho_{00}^{GJ} = \rho_{10}^{GJ} = \rho_{1-1}^{GJ} = 0$ [30].

It is clear that knowing the ρ elements in one frame, one can immediately calculate them in any other frame by a Wigner rotation. The y -axis is always the normal to the vector meson production plane; $\vec{y} = \vec{k} \times \vec{q}$, where \vec{k} is the incoming photon direction and \vec{q} is the outgoing vector meson (ϕ) direction. The choice of the z -axis is frame dependent, as described above. For the Adair frame $\vec{z} = \vec{k}$, for the Helicity frame, $\vec{z} = \vec{q}$, and for the GJ frame, $\vec{z} = \vec{k}'$, where \vec{k}' points along the incoming photon direction in the vector meson rest frame. Once the y - and the z -axis has been fixed, $\vec{x} = \vec{y} \times \vec{z}$. Let $\hat{\pi}$ be the direction of the daughter K (for $\phi \rightarrow KK$) in the chosen reference frame. Then the angles ζ and φ in

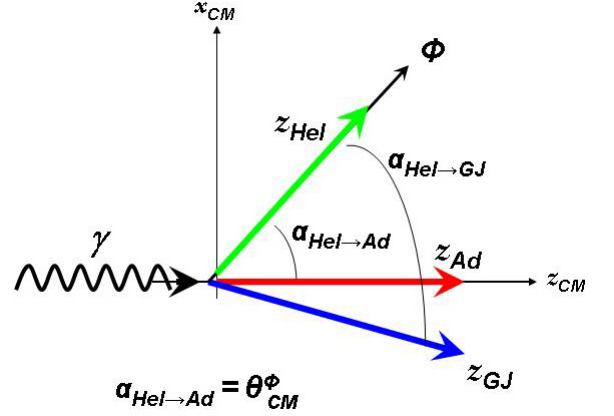


FIG. 9: (Color On-line) The spin-quantization axes for the Helicity (Hel, in green), Adair (Ad, in red) and Gottfried-Jackson (GJ, in blue) frames, in relation to the overall center-of-mass ($c.m.$) frame. The z -axis for the overall $c.m.$ frame points along the beam direction and coincides with z_{Ad} . Since z_{Hel} points along the direction of the ϕ meson, the angle between the Helicity and Adair frames is just $\theta_{c.m.}^\phi$. The Gottfried-Jackson frame is defined as the direction of the incoming photon, as seen in the rest frame of the ϕ meson. The angle between the Helicity and Gottfried-Jackson frame is given by Eq. 27b.

Eq. 23 are given as [29]:

$$\cos \zeta = \hat{\pi} \cdot \hat{z}, \quad \cos \varphi = \frac{\hat{y} \cdot (\hat{z} \times \hat{\pi})}{|\hat{z} \times \hat{\pi}|}, \quad \sin \varphi = -\frac{\hat{x} \cdot (\hat{z} \times \hat{\pi})}{|\hat{z} \times \hat{\pi}|}. \quad (24)$$

In the Rose convention of the signs (this is the followed by Schilling in Ref. [29]), the Wigner rotation matrix for a spin-1 system is

$$d^1(\alpha) = \begin{pmatrix} \frac{1}{2}(1 + \cos \alpha) & -\frac{1}{\sqrt{2}} \sin \alpha & \frac{1}{2}(1 - \cos \alpha) \\ \frac{1}{\sqrt{2}} \sin \alpha & \cos \alpha & -\frac{1}{\sqrt{2}} \sin \alpha \\ \frac{1}{2}(1 - \cos \alpha) & \frac{1}{\sqrt{2}} \sin \alpha & \frac{1}{2}(1 + \cos \alpha) \end{pmatrix}. \quad (25)$$

To rotate the density matrix from reference frame A to B , the transformation is

$$\rho^B = d^1(-\alpha_{A \rightarrow B}) \rho^A d^1(\alpha_{A \rightarrow B}). \quad (26)$$

The rotation angles (counter-clockwise is positive) are given by [29]

$$\alpha_{Ad \rightarrow Hel} = \theta_{c.m.}^\phi, \quad (27a)$$

$$\alpha_{Hel \rightarrow GJ} = -\cos^{-1} \left(\frac{\beta - \cos \theta_{c.m.}^\phi}{\beta \cos \theta_{c.m.}^\phi - 1} \right) \quad (27b)$$

$$\alpha_{Ad \rightarrow GJ} = \alpha_{Ad \rightarrow Hel} + \alpha_{Hel \rightarrow GJ}, \quad (27c)$$

where $\beta = |\vec{p}_K|/E_K$ is the velocity of the daughter kaon in the ϕ rest frame (for the $\phi \rightarrow KK$ decay).

B. “PWA” method and “Schilling’s” method of SDME extraction in the Adair frame

The expansion of the production amplitudes using partial wave analysis (PWA) techniques in Sec. ?? allows for an elegant way of extracting the spin density matrix elements (SDME’s). For this, we follow Schilling [29] and express the SDME’s in terms of the production amplitudes as

$$\rho_{m_\phi m'_\phi} = \frac{\sum_{m_f m_\gamma m_i} \mathcal{A}_{m_\phi m_f m_i m_\gamma} \mathcal{A}_{m'_\phi m_f m_i m_\gamma}^*}{\sum_{m_\phi m_f m_\gamma m_i} |\mathcal{A}_{m_\phi m_f m_i m_\gamma}|^2}, \quad (28)$$

where $\mathcal{A}_{m_\phi m_f m_i m_\gamma}$ are the same amplitudes as in the PWA fit in Sec. ??, and m_γ , m_i and m_f and m_ϕ are the spins of the incoming photon, target proton, outgoing proton and the ϕ vector meson, respectively. Note that the $\phi \rightarrow KK$ decay portion of the full amplitude in Eq. ?? occurs a constant factor that cancels between the numerator and the denominator in Eq. 28. The ϕ decay portion of the full amplitude in Eq. ?? can therefore be suppressed for SDME extraction.

The above “PWA” method is completely equivalent to a direct application of the Schilling’s expression for the intensity given by Eq. 23 (“Schilling’s” method). Since the spin-quantization axis for our PWA amplitudes was along the beam direction, the PWA method of extraction yields results in the Adair frame. The PWA expansion was specifically tuned to represent distributions in all kinematic variables, in particular, the intensity distribution given by Eq. 23. Fig. 10 shows a comparison of the results using the two methods for the charged-mode topology; the agreement is excellent. The final results for the ρ elements we present in this analysis use the PWA method only.

X. RESULTS

A. Differential cross sections

Figs. 11-13 show our differential cross section results in different angular bins for the charged-mode topology with the $\Lambda(1520)$ hard cut, while Fig. 14 shows that same for the neutral-mode topology. The energy binning for the charged-mode is uniformly 10-MeV-wide, while the minimum bin-width for the neutral-mode is 30-MeV-wide. At higher energies and backward-angles, the neutral-mode has very limited statistics and no results are reported in these kinematic regimes. We also do not report cross section results for the bins $\sqrt{s} = 2.735$ and 2.745 GeV due to the normalization issues, as described in Sec.

Figs. 15 and 16 show the comparison between the charged- and neutral-mode differential cross section results. In keeping with the diffractive nature of vector

meson photoproduction, we have chosen to present our results as $d\sigma/dt$ here, with the conversion being

$$\frac{d\sigma}{dt} = \frac{1}{2} \left(\frac{1}{E_\gamma |\vec{p}_\phi|} \right)_{c.m.} \left(\frac{d\sigma}{d \cos \theta_{c.m.}^\phi} \right). \quad (29)$$

The diffractive Pomeron exchange mechanism is clearly borne out in the very forward-most angular bin ($t \rightarrow 0$), where $d\sigma/dt$ remains almost constant above $\sqrt{s} > 2.3$ GeV. The structure around $\sqrt{s} \approx 2.1$ GeV is clearly present in both topologies. Above $\sqrt{s} > 2.3$ GeV, the two topologies are in very good agreement, except in the $\cos \theta_{c.m.}^\phi = 0.7$ and 0.8 bins, where the neutral-mode cross sections tend to be slightly lower.

B. Comparison with previous world data

Previous world data for ϕ photoproduction cross sections are generally scarce and no world data exists for the neutral-mode topology at all. We therefore restrict our discussion to the charged-mode topology only. For low energy and forward-angle kinematics, there are two previous results from the SAPHIR (2003, Barth *et al.* [9]) and LEPS (2004, Mibe *et al.* [10]) Collaborations. Both data sets have wide energy binnings, $E_\gamma \approx 200$ -MeV-wide and 100-MeV-wide bins for SAPHIR and LEPS, respectively. However, the common feature in both results is of a prominent enhancement around $E_\gamma \approx 2$ GeV ($\sqrt{s} \approx 2.2$ GeV) in the forward-angle $d\sigma/dt$, in agreement with our current results.

Since the SAPHIR and LEPS kinematics was mostly at forward-angles, these results were presented as $d\sigma/dt$ *vs.* $|t - t_0|$, where t_0 was the value of t at $\theta_{c.m.}^\phi = 0$. From the phenomenology of diffractive production, $d\sigma/dt$ was expected to show a simple exponential fall off with $|t - t_0|$. The conversion of $\cos \theta_{c.m.}^\phi$ to t or $|t - t_0|$ depends on \sqrt{s} . With a wide energy bins, it is not immediately clear which \sqrt{s} should be chosen for this conversion. Therefore, we convert our results in to the units chosen by SAPHIR and LEPS and make independent comparisons with both of them. Since our energy binning is much finer (10-MeV-wide in \sqrt{s}), we overlay our results at the energy bin-center of the SAPHIR or LEPS results. Figs. 17 and 18 show the comparison between our results with SAPHIR and LEPS, respectively.

The only existing world data for large $|t|$ are the CLAS (2000, Anciant *et al.* [12]) results for a bin-center at $E_\gamma = 3.6$ GeV (tagged photon energy range 3.3 to 3.9 GeV). The chief motivation of the previous CLAS experiment was to investigate whether u -channel processes (at small u or large t) contribute to the ϕ channel. Assuming that the ϕ is almost pure $s\bar{s}$ and the strangeness content in ordinary nucleons is small, the coupling constant $g_{\phi NN}$ is expected to be small and therefore nucleon exchanges in the u -channel are supposed to be suppressed. However, as shown in Fig. 19, both the CLAS 2000 and the current CLAS 2010 results show a small

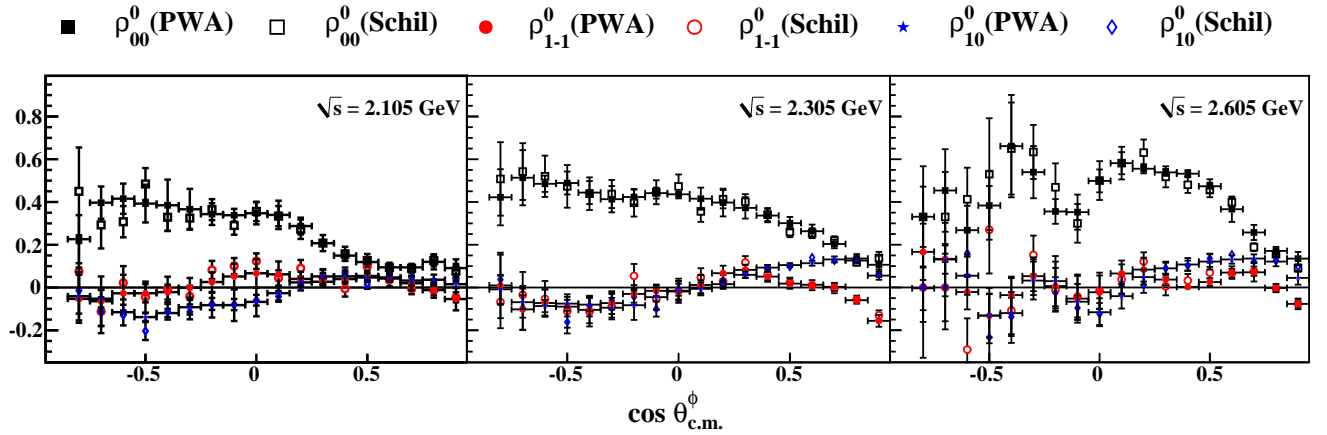


FIG. 10: (Color On-line) Compare

but distinct rise in the backward-angles, suggestive of a non-negligible value for $g_{\phi NN}$.

Lastly, we compare our results with the $E_\gamma = 3.3$ GeV bin-center results from Daresbury (1982, Barber *et al.* [6])

C. Spin density matrix elements

Figs. 21-23 show the spin density matrix elements (SDME) for the charged-mode topology (including the $\Lambda(1520)$ hard cut) in the Adair frame. The most prominent feature is the large value of ρ_{00} , while ρ_{10} and ρ_{1-1} are small, but non-zero. There is a similarity with the corresponding results for the ωp channel [14] in the “hump-like” structure for ρ_{00} . At high \sqrt{s} , the ωp results had a distinct “dip” for ρ_{00} in the mid-forward angles. For the ϕp case, there are indications of a “dip” for ρ_{00} in the mid- to mid-backward angles, though the structure is much less well-defined due to statistical limitations at high \sqrt{s} and $\cos \theta_{c.m.}^\phi < 0$.

Fig. 26 shows the SDME’s for the neutral-mode topology in the Adair frame. The energy bins are at least 30-MeV-wide in \sqrt{s} . Fig shows comparisons between the charged- and neutral-mode SDME results for the ρ_{00} element.

XI. PHYSICS DISCUSSION

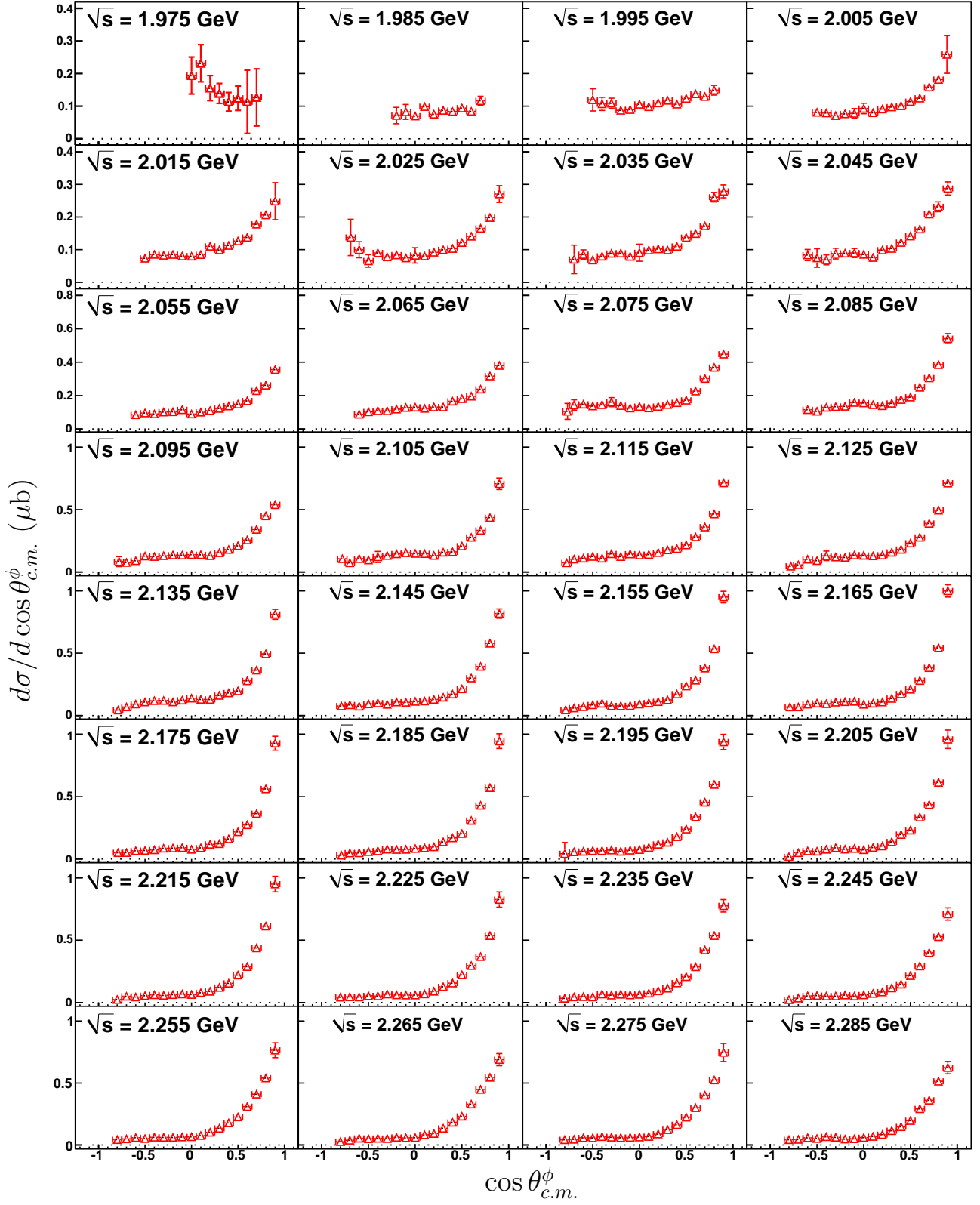


FIG. 11: (Color On-line) $\frac{d\sigma}{d \cos \theta_{c.m.}^\phi}$ (μb) vs. \sqrt{s} : Differential cross section results for the charged-mode topology in the energy range $1.97 \text{ GeV} \leq \sqrt{s} < 2.29 \text{ GeV}$. The centroid of each 10-MeV-wide bin is printed on the plots. The y-axis range is constant over each horizontal row and is shown in the left-most column for every row. All error bars represent statistical uncertainties only.

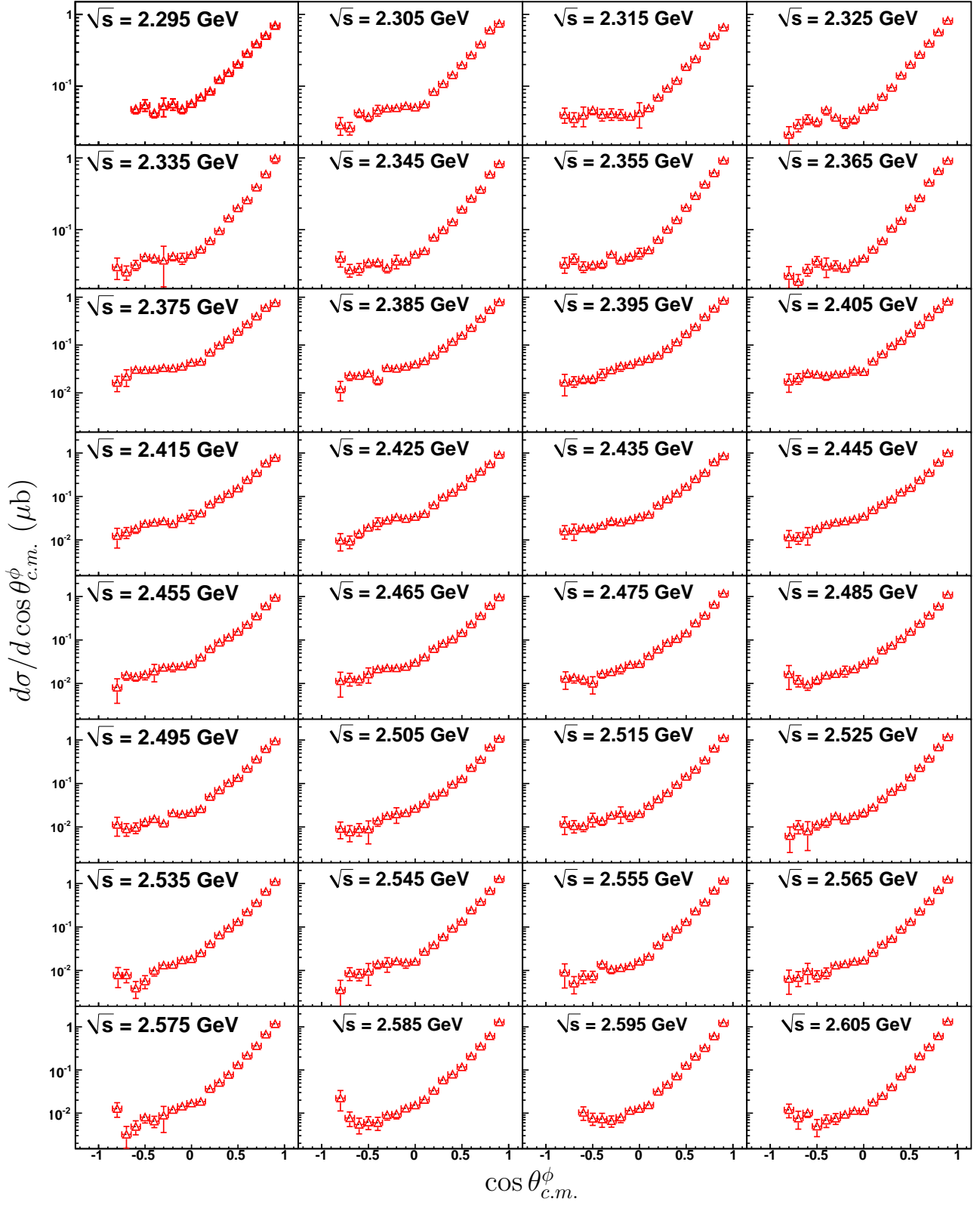


FIG. 12: (Color On-line) $\frac{d\sigma}{d \cos \theta_{c.m.}^\phi}$ (μb) vs. \sqrt{s} : Differential cross section results for the charged-mode topology in the energy range $2.29 \text{ GeV} \leq \sqrt{s} < 2.61 \text{ GeV}$. The centroid of each 10-MeV-wide bin is printed on the plots. The y-axis range is constant over each horizontal row and is shown in the left-most column for every row. All error bars represent statistical uncertainties only.

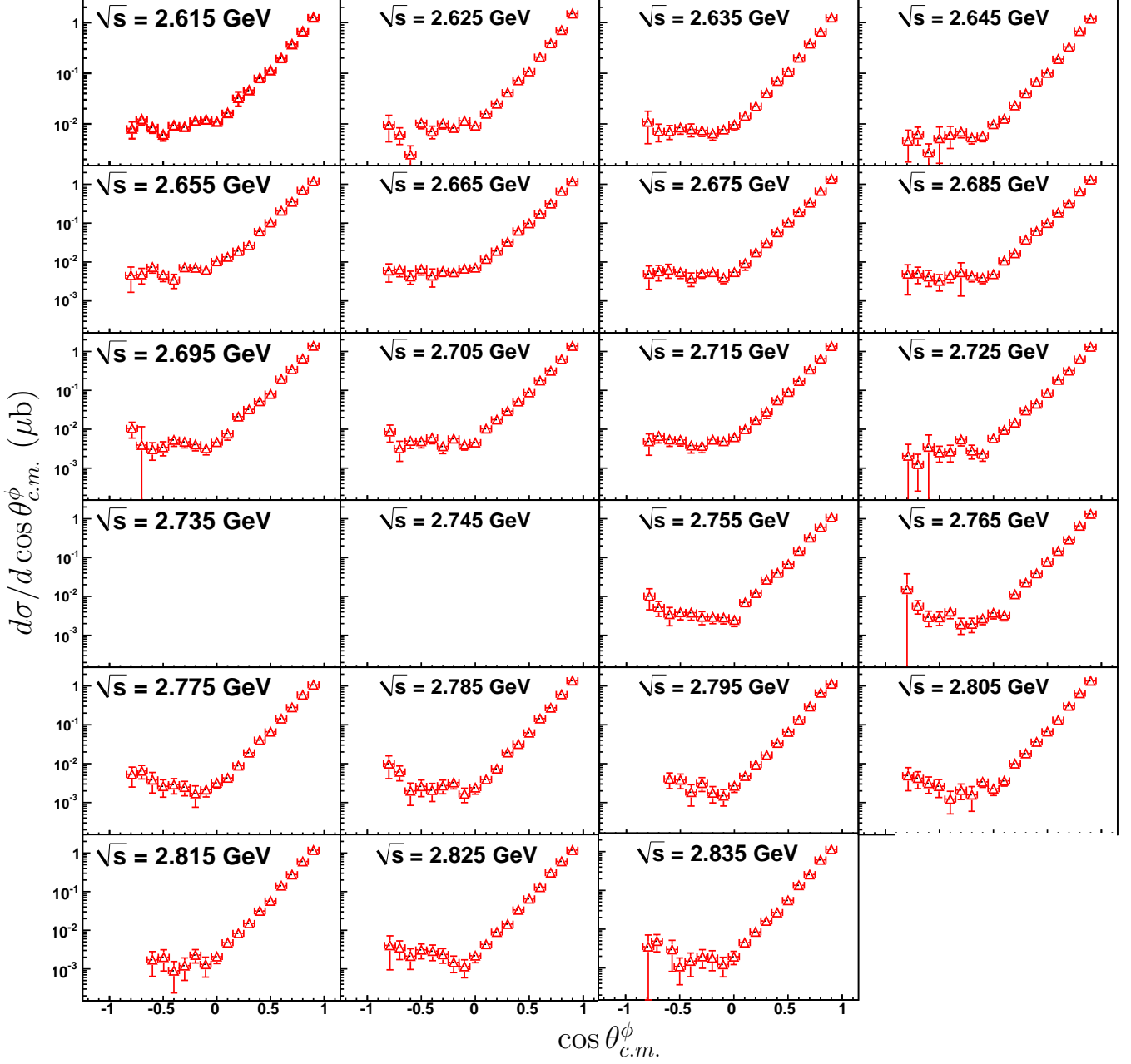


FIG. 13: (Color On-line) $\frac{d\sigma}{d \cos \theta_{c.m.}^{\phi}}$ (μb) vs. \sqrt{s} : Differential cross section results for the charged-mode topology in the energy range $2.61 \text{ GeV} \leq \sqrt{s} < 2.84 \text{ GeV}$. The centroid of each 10-MeV-wide bin is printed on the plots. The y-axis range is constant over each horizontal row and is shown in the left-most column for every row. No results are presented for the bins $\sqrt{s} = 2.735$ and 2.745 GeV due to the normalization issues, as described in Sec. All error bars represent statistical uncertainties only.

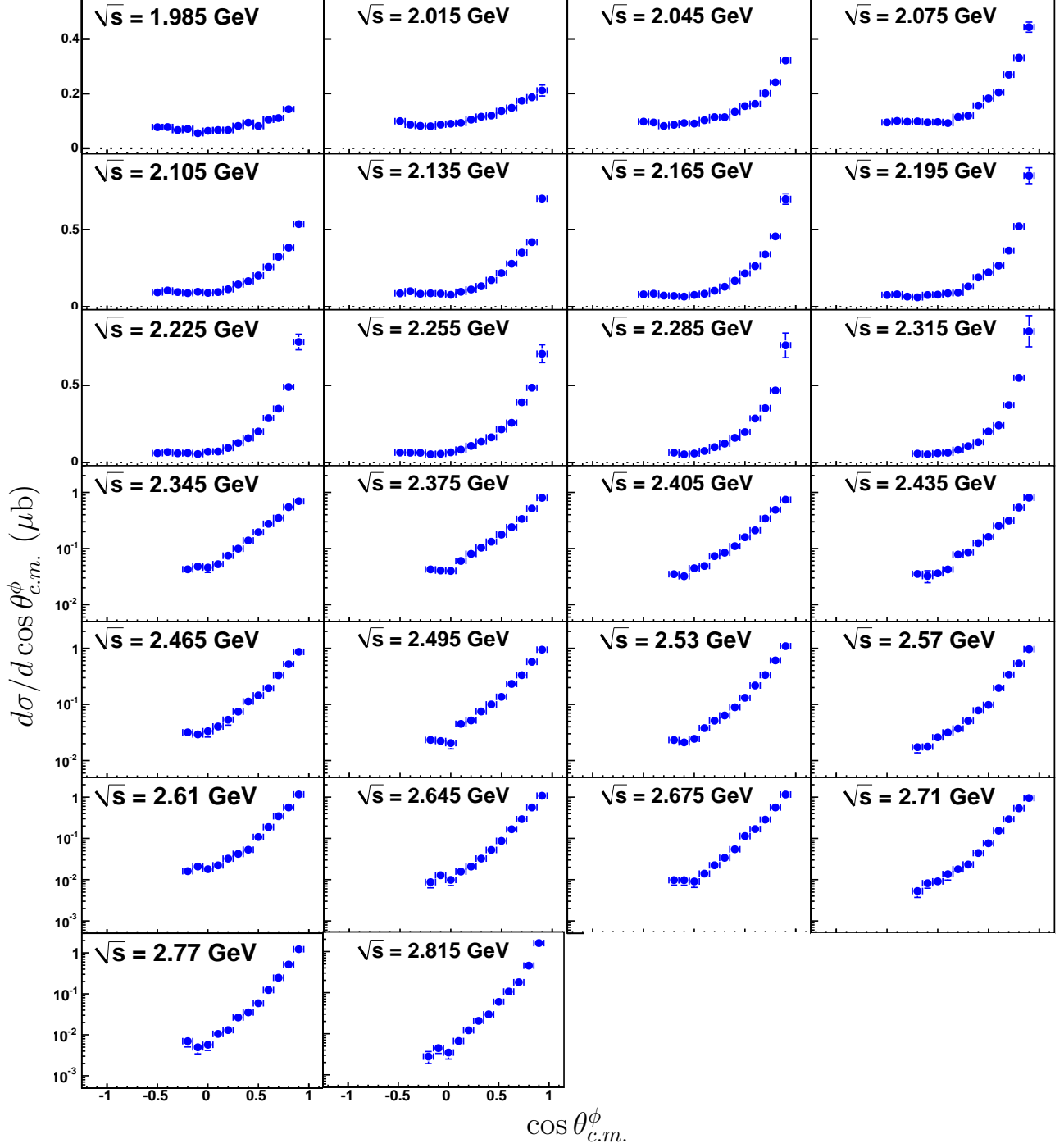


FIG. 14: (Color On-line) $\frac{d\sigma}{d \cos \theta_{c.m.}^\phi}$ (μb) vs. \sqrt{s} : Differential cross section results for the neutral-mode topology. The minimum bin-width is 30-MeV and the bin-centroid is printed on the plots. The y-axis range is constant over each horizontal row and is shown in the left-most column for every row. All error bars represent statistical uncertainties only.

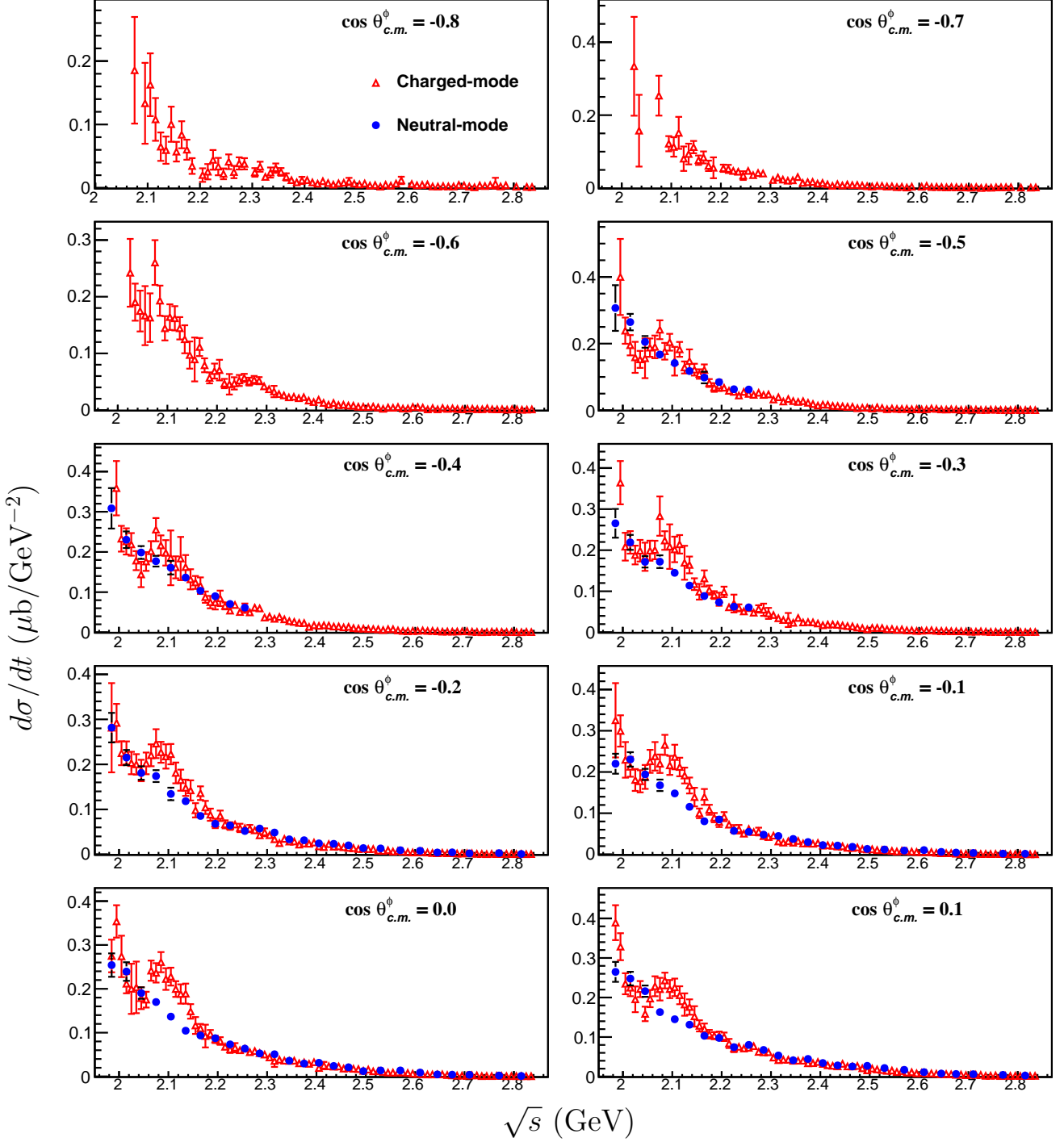


FIG. 15: (Color On-line) Comparison of the charged- and neutral-mode $d\sigma/dt$ results in the mid- and backward-angle bins. There is a prominent difference between the two results around $\sqrt{s} \approx 2.1$ GeV, especially in the mid-angle regions. All error bars represent statistical uncertainties only.

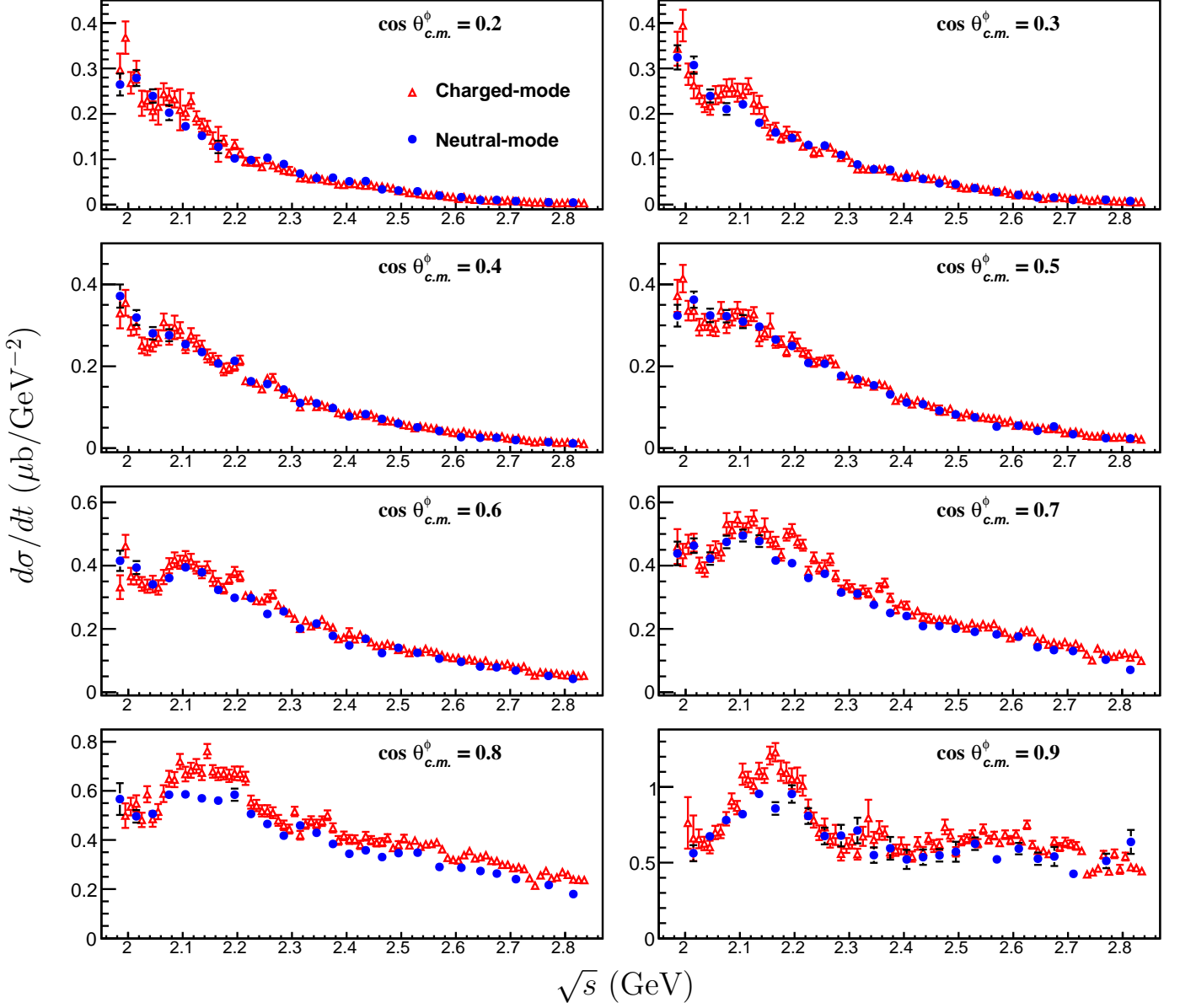


FIG. 16: (Color On-line) Comparison of the charged- and neutral-mode $d\sigma/dt$ results in the mid- and forward-angle bins. There is a prominent difference between the two results around $\sqrt{s} \approx 2.1$ GeV, especially in the mid-angle regions. Both topologies show the $\sqrt{s} \approx 2.1$ GeV structure in the forward-most angular bins. $d\sigma/dt$ appears almost constant above $\sqrt{s} \approx 2.3$ GeV for $\cos \theta_{c.m.}^\phi = 0.9$ ($t \rightarrow 0$), as expected for diffractive photoproduction. All error bars represent statistical uncertainties only.

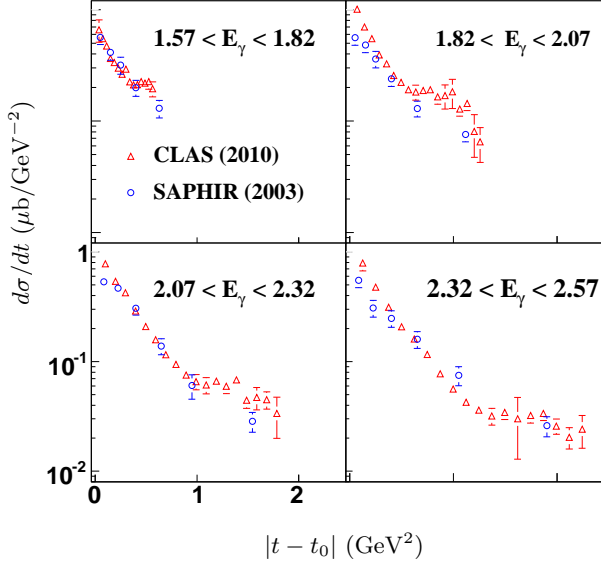


FIG. 17: (Color On-line) Comparison between the present CLAS 2010 (red triangles) and 2003 SAPHIR 2003 [9] (blue circles) results. The SAPHIR binning in E_γ (GeV) is printed on each pad and the CLAS results are at the bin-centers for each SAPHIR energy bin. The CLAS results are taken from the charged-mode topology (including the $\Lambda(1520)$ hard cut). All error bars represent statistical uncertainties only.

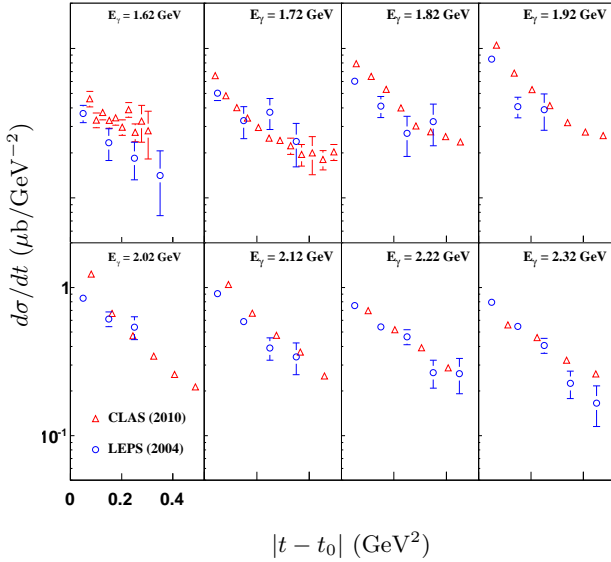


FIG. 18: (Color On-line) Comparison between the present CLAS 2010 (red triangles) and LEPS 2004 [10] (blue circles) results. The LEPS data had $E_\gamma = 200$ MeV wide bins (the bin-center is printed on each pad). The present CLAS results are taken from the charged-mode topology (including the $\Lambda(1520)$ hard cut). All error bars represent statistical uncertainties only.

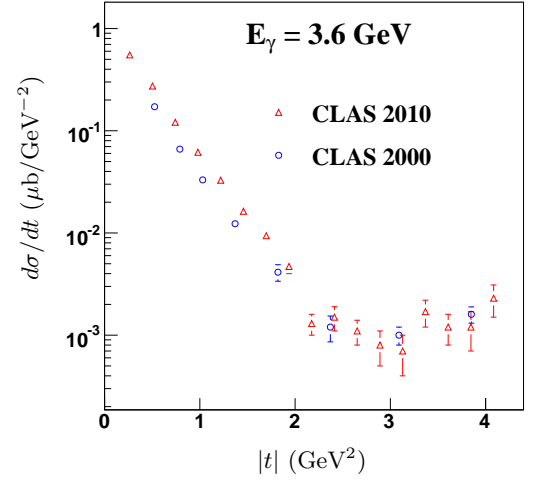


FIG. 19: (Color On-line) Comparison between the current CLAS (red triangles) and 2000 CLAS [12] (blue circles) results at the energy bin-center $E_\gamma = 3.6$ GeV. The CLAS 2000 energy binning was 600-MeV in E_γ while the current CLAS binning is 10-MeV-wide in \sqrt{s} .

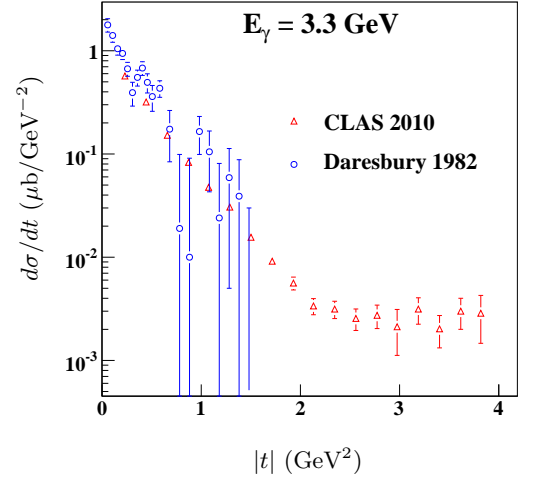


FIG. 20: (Color On-line) Comparison between the current CLAS (red triangles) and 1982 Daresbury [6] (blue circles) results at the bin-center $E_\gamma = 3.3$ GeV. The Daresbury energy bins were 1-GeV-wide in E_γ while the CLAS binning is 10-MeV-wide in \sqrt{s} .

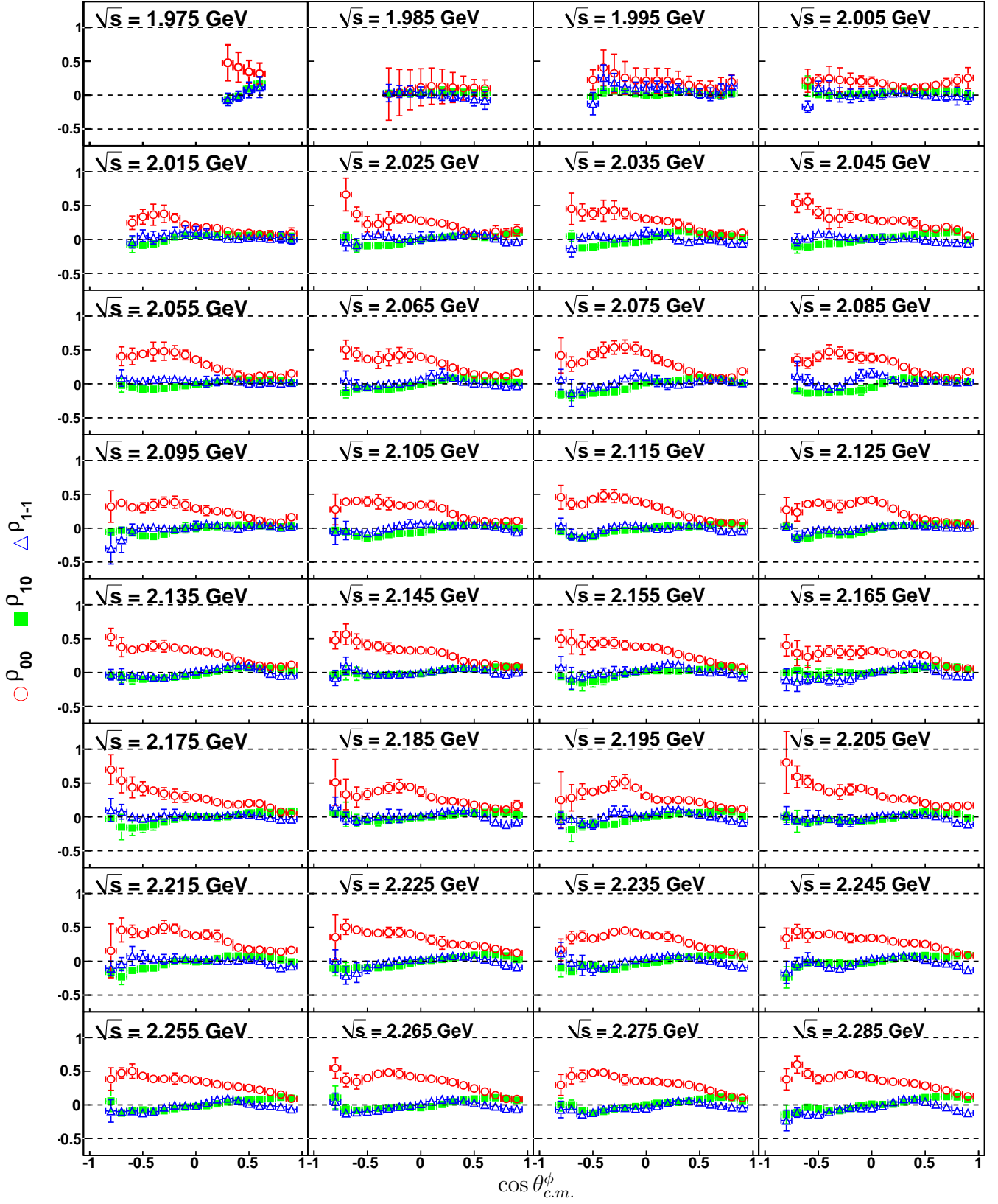


FIG. 21: (Color On-line) SDME *vs.* $\cos \theta_{c.m.}^\phi$: spin density matrix elements in the Adair frame for the charged-mode topology (with $\Lambda(1520)$ hard cut) in the energy range $1.97 \text{ GeV} \leq \sqrt{s} < 2.29 \text{ GeV}$. The centroid of each 10-MeV-wide bin is printed on the plots. All error bars represent statistical uncertainties only.

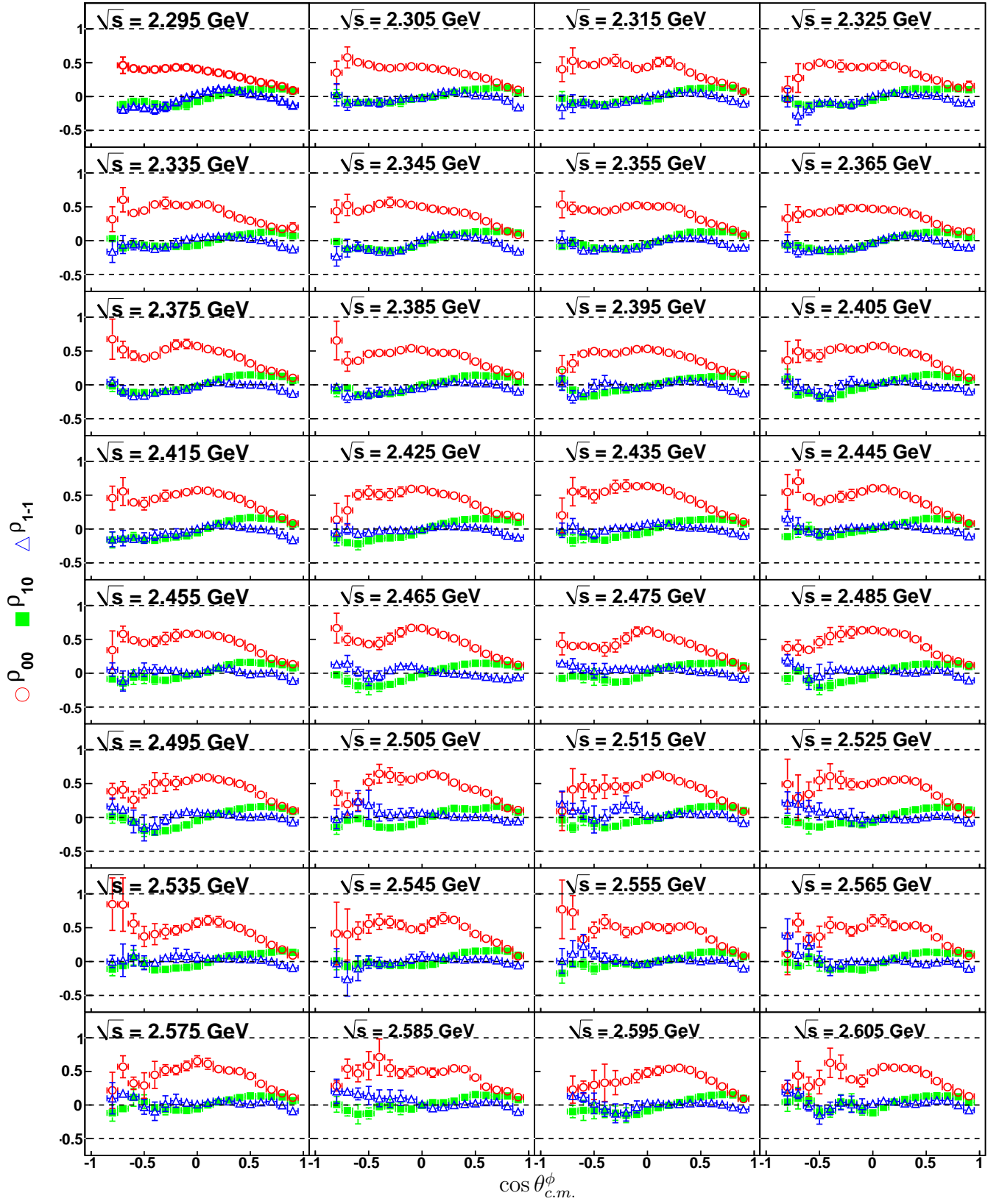


FIG. 22: (Color On-line) SDME *vs.* $\cos \theta_{c.m.}^\phi$: spin density matrix elements in the Adair frame for the charged-mode topology with the $\Lambda(1520)$ hard cut in the energy range $2.29 \text{ GeV} \leq \sqrt{s} < 2.61 \text{ GeV}$. The centroid of each 10-MeV-wide bin is printed on the plots. All error bars represent statistical uncertainties only.

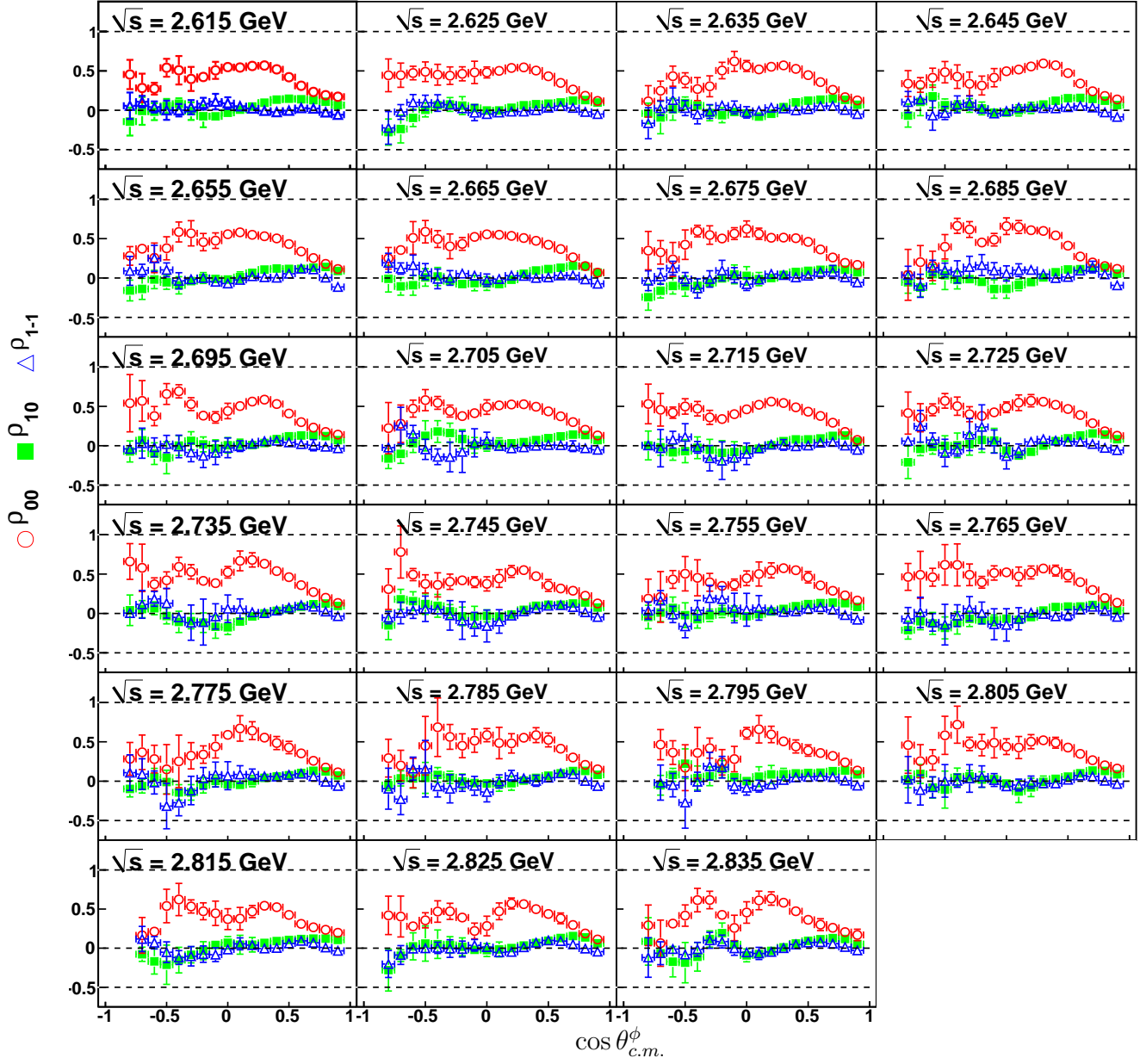


FIG. 23: (Color On-line) SDME *vs.* $\cos \theta_{c.m.}^\phi$: spin density matrix elements in the Adair frame for the charged-mode topology with the $\Lambda(1520)$ hard cut in the energy range $2.61 \text{ GeV} \leq \sqrt{s} < 2.84 \text{ GeV}$. The centroid of each 10-MeV-wide bin is printed on the plots. All error bars represent statistical uncertainties only.

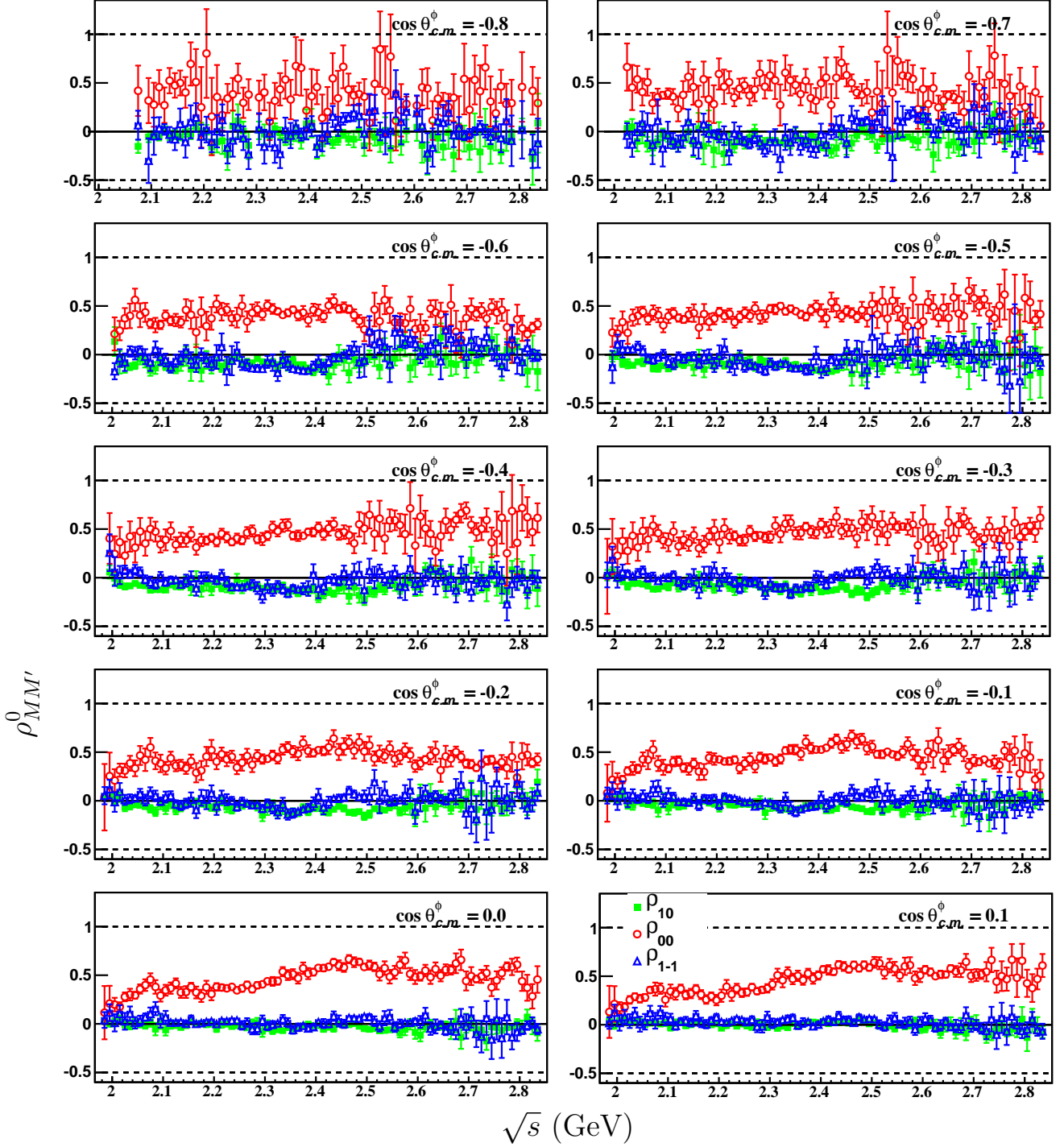


FIG. 24: (Color On-line) The energy dependence of SDME's (Adair frame) in the backward-angle bins for the charged-mode topology. All error bars represent statistical uncertainties only.

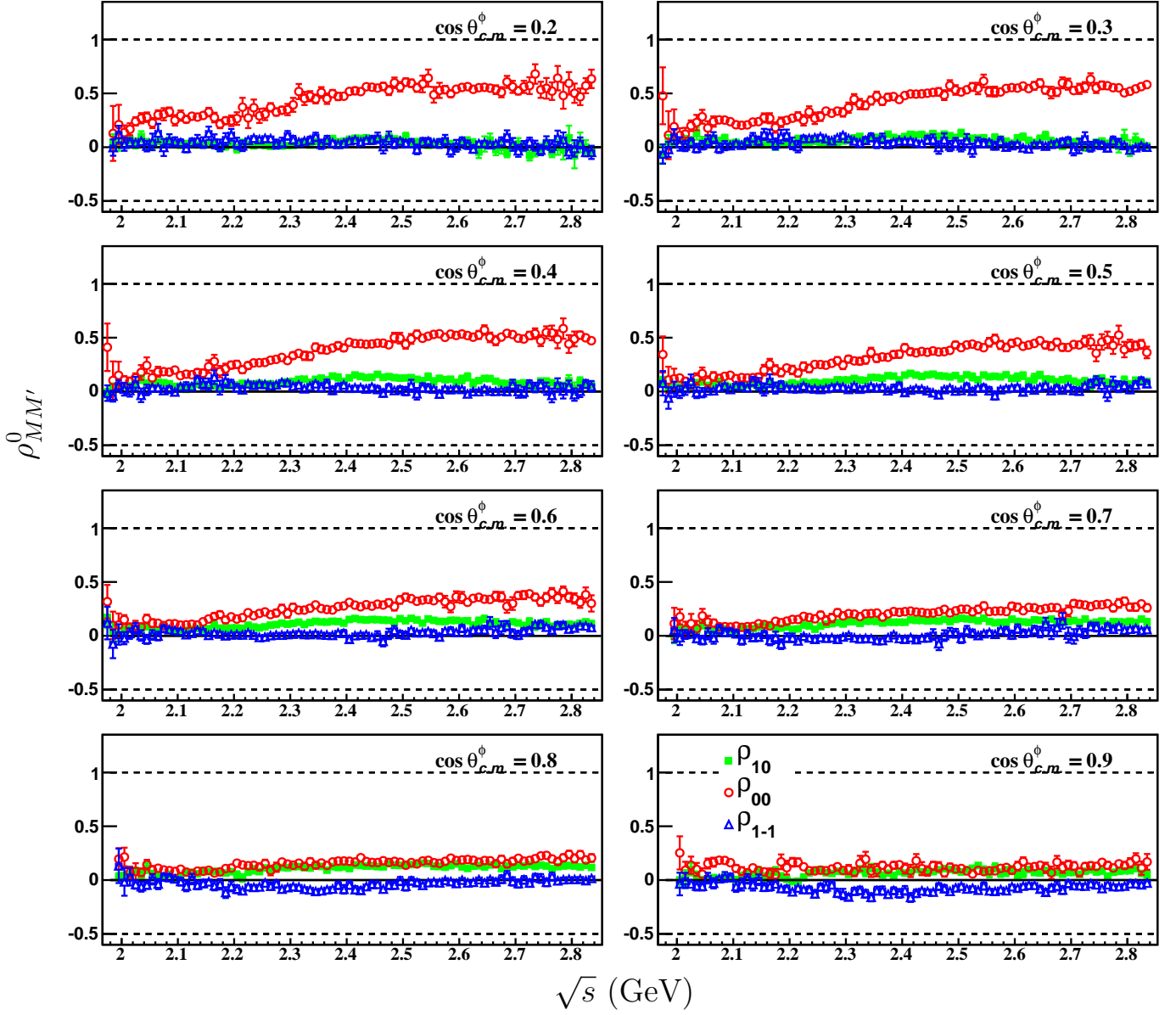


FIG. 25: (Color On-line) The energy dependence of SDME's (Adair frame) in the mid- and forward-angle bins for the charged-mode topology. All error bars represent statistical uncertainties only.

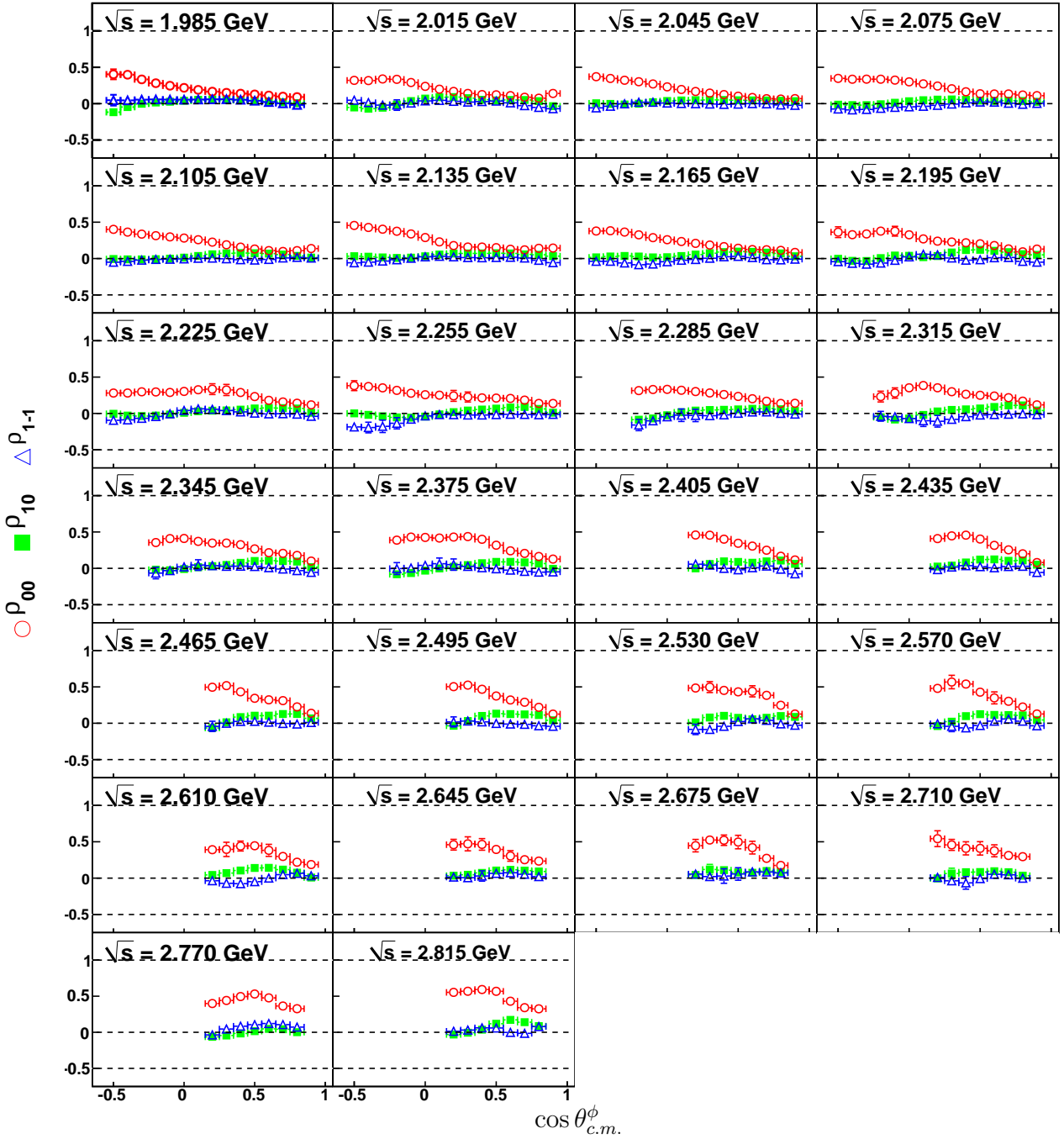


FIG. 26: (Color On-line) SDME *vs.* $\cos \theta_{c.m.}^\phi$: spin density matrix elements in the Adair frame for the neutral-mode topology. The minimum bin-width is 30-MeV in \sqrt{s} and the centroid of each bin is printed on the plots. All error bars represent statistical uncertainties only.

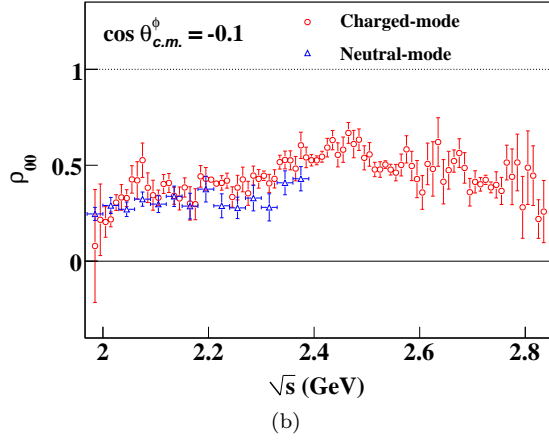
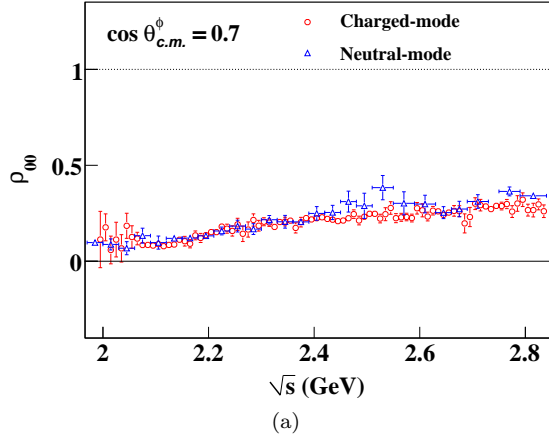


FIG. 27: (Color On-line) Comparison between the charged- and neutral-mode ρ_{00} results in the Adair frame at (a) forward- and (b) mid-angle regions. While the agreement is generally good in most kinematic regimes, the charged-mode shows traces of a “structure” around $\sqrt{s} \approx 2.1$ GeV in the mid-angle regions. This is coincident with a similar feature for the differential cross sections, though the effect seems to be less prominent for the SDME’s.

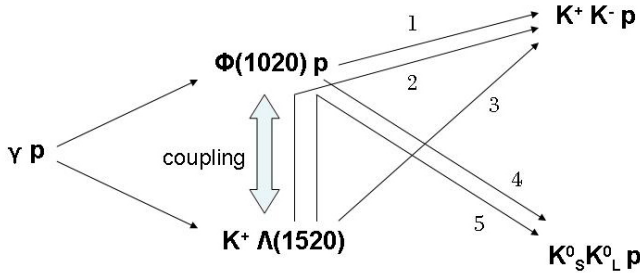


FIG. 28: (Color On-line) If ϕ - $\Lambda(1520)$ coupling is allowed, the charged-mode case has three “paths” (enumerated as 1, 2 and 3) to its final-state, while the neutral-mode has two “paths” (enumerated as 4 and 5) to its final state.

A. ϕ - $\Lambda(1520)$ interference

As explained earlier in Sec. IV C, for \sqrt{s} between 2 and 2.2 GeV, the ϕp and $K^+\Lambda(1520)$ channels can kinematically overlap in phase space if they have the same K^+ , K^- and proton final-state particle configuration. For the ϕ channel, this corresponds to the charged-mode topology. Therefore any effect of the $K^+\Lambda(1520)$ channel on ϕp photo-production is expected to be enhanced for the charged-mode. Furthermore, from our discussion in Sec. V, the ϕ - $\Lambda(1520)$ there is also a strong angular dependence in this overlap, the mid-angle regions showing the maximal enhancement. This also corroborates with the general observation that our differential cross section and SDME results from the charged- and neutral-mode topologies differ only in the specific kinematic region of mid-angles and \sqrt{s} between 2 and 2.2 GeV. Fig. 15 illustrates this for the differential cross sections and Fig. 27b shows the case for ρ_{00} element.

In conjunction with the fact that the charged- and neutral-mode results seem to differ in those kinematic regimes where the ϕ - $\Lambda(1520)$ overlap in phase-space is most favored, clearly, even the neutral-mode topology shows a sharp “structure” around $\sqrt{s} \approx 2.2$ GeV. The pertinent question thus arises wheether the $\Lambda(1520)$ can play a role a role even in the neutral-mode case. Recently, Ozaki and co-workers [31] have postulated that the $\Lambda(1520)$ and ϕ couples dynamically, and this can give rise to the 2.2 GeV structure. If this is the case, then indeed, this structure should show up in both the charged- and neutral-mode topologies.

It is therefore possible that there are two separate phenomena occurring here. Firstly, the ϕ - $\Lambda(1520)$ couples dynamically. This happens at the production amplitude level and is an interference effect. Since this should affect the neutral-mode as well, and the neutral-mode differential seem to have the 2.2 GeV structure only in the forward-most angular bins, the interference should also be peaked at the forward-angles as well. Secondly, there is an effect from the kinematic overlap in phase space between the $K^+\Lambda(1520)$ and ϕp charged-mode topology. The latter effect should be less of a dynamical nature

and we explicitly distinguish between the terms “interference” and “overlap”, though it is possible that the two phenomena convolute in some fashion. However, what is clear is that the dynamical interference should apply to both the charged- and neutral-mode topologies, while the effect from the overlap should have a minimal effect on the neutral-mode. Fig. 28 illustrates the effect of the $\Lambda(1520)$ on the two topologies. Consider the process $\gamma p \rightarrow X \rightarrow KKp$, where the KK refers to either K^+K^- (charged-mode) or $K_S^0 K_L^0$ (neutral-mode), and X refers to a generic intermediate state comprising of ϕp and $K^+\Lambda(1520)$. If ϕ - $\Lambda(1520)$ coupling is allowed, the charged-mode case has three “paths” to the final-state, while the neutral-mode has two “paths” and this can account for the difference in the two results. However, a deeper theoretical investigation is required to obtain a full dynamical picture of the production processes.

B. Diffractive exchange parameters B_ϕ and C_ϕ

As mentioned in the introductory section, the ϕ photoproduction channel is ideally suited to study the phenomenology of Pomeron exchange in the diffractive limit of $t \rightarrow t_0$, where $t_0 = |t|_{min}$ corresponds to $\cos \theta_{c.m.}^\phi = 0$ for a given \sqrt{s} . The Pomeron Regge trajectory is approximately given by $\alpha(t) \approx 1.08 + 0.25t$ where $d\sigma/dt$ scales as $\sim (\beta(t)s^{\alpha(t)})^2/s^2$ and $\beta(t)$ is the Regge residue that behaves like a form-factor. Therefore, in the diffractive limit of small t and large s , $d\sigma/dt$ should show a very slow variation with s . We pointed out this signature in Sec. XA, where $d\sigma/dt$ was approximately constant in the forward-most angular bin, above $\sqrt{s} \approx 2.3$ GeV.

Such diffractive Pomeron exchanges is expected to occur for all three vector mesons ρ , ω and ϕ . However, for the ρ and ω , additional meson exchanges occur as well. For the ω , t -channel π exchanges are thought to have a more dominant contribution than the Pomeron. Since the ϕ is almost purely $s\bar{s}$, such light-quark π exchanges are suppressed and diffractive Pomeron exchange is the dominant contribution to the production amplitude. In the VMD model, the photoproduction cross section can be related to the elastic scattering cross section as

$$\frac{d\sigma}{dt}(\gamma p \rightarrow \phi p) \approx \frac{\alpha}{4} \frac{4\pi}{\gamma_\phi^2} \left(\frac{|\vec{p}_\phi|}{E_\gamma} \right)_{c.m.}^2 \frac{d\sigma}{dt}(\phi p \rightarrow \phi p) \quad (30)$$

where γ_ϕ is the photon- ϕ coupling constant. For Pomeron exchanges, the form-factor $\beta(t)$ is generally taken as $\exp(-B_\phi(|t-t_0|))$ and Eq. 30 can be recast in the form

$$\frac{d\sigma}{dt}(\gamma p \rightarrow \phi p) = C_\phi \left(\frac{|\vec{p}_\phi|}{E_\gamma} \right)_{c.m.}^2 \exp(-B_\phi(|t-t_0|)), \quad (31)$$

with the parameters B_ϕ and C_ϕ expected to be approximately energy-independent. Fig. 29a shows the variation of the extracted slope parameter B_ϕ for the two topologies. There are several features of note here. Above

$\sqrt{s} \approx 2.3$ GeV, B_ϕ has an almost constant value of 3 GeV^{-2} , and this is true for both the topologies. This value of $B_\phi \approx 3 \text{ GeV}^{-2}$ is consistent with the result from Daresbury [6]. Below $\sqrt{s} \approx 2.3$ GeV, especially around $\sqrt{s} \approx 2.1$ GeV, the two topologies give different results and both of them show a distinctly large deviation from $B_\phi \approx 3 \text{ GeV}^{-2}$, possibly due to effects from the $\Lambda(1520)$. Fig. 29b shows the variation of the extracted slope parameter C_ϕ for the two topologies with \sqrt{s} . In the ϕ - $\Lambda(1520)$ interference region below $\sqrt{s} \approx 2.2$ GeV, the sharp rise in C_ϕ with decreasing \sqrt{s} points to the possibility that the simple diffractive Pomeron picture given by Eq. 31 is no longer valid in this kinematic regime. The overall trend at higher energies ($\sqrt{s} > 2.3$ GeV) is $C_\phi \approx 1.9 \text{ } \mu\text{bGeV}^{-2}$.

C. Helicity non-conservation and ρ_{00}

If we ignore the spin-indices of the target- and outgoing-proton which we do not measure, in Eq. 28, the definition of ρ_{00} becomes

$$\rho_{00} \sim |\mathcal{A}_{m_\phi=0, m_\gamma=1}|^2 + |\mathcal{A}_{m_\phi=0, m_\gamma=-1}|^2. \quad (32)$$

Therefore, a non-zero value of ρ_{00} is a direct measure of helicity flips between the incoming photon and the outgoing vector-meson. Although we have presented our SDME results in the Adair frame, these can easily be

converted in to the Helicity and Gottfried-Jackson frames by applying Wigner rotations, as described in Sec. IX A. Doing so, one finds that ρ_{00} is distinctly large at most kinematics, in all the three reference frames (the Adair-frame results were shown in Sec. XB). The problem arises because in the simplest diffractive picture, the energy dependence of the exchanged particle is that of a scalar [30], which should not cause helicity flips. However, Gilman *et al.* [30] postulated that TCHC should be badly broken, but SCHC should hold. Fig. 30 shows the ρ_{00} element for the charged-mode topology in the forward-most angular bins for all three reference frames. Indeed, ρ_{00}^{GJ} is large and TCHC is strongly violated, while ρ_{00}^{Hel} is relatively small, indicating that SCHC violation occurs to a lesser degree than TCHC violation.

D. Comparison with ω and $R_{\phi/\omega}$

Fig. 31 shows the ratio between the differential cross sections for ϕp and ωp photoproduction ($R_{\phi/\omega}$). Typically, the ratio is small, as expected from an OZI perspective, where $R_{\phi/\omega} = \tan^2 \Delta\theta_V \approx 4.2 \times 10^{-3}$ [17]. However, towards higher \sqrt{s} and forward-angles $R_{\phi/\omega}$, $R_{\phi/\omega}$ is found to be large. This is in agreement with the results in Ref. [17] and points towards a common Pomeron exchange mechanism.

-
- [1] J. J. Sakurai, *Currents and Mesons*, The University of Chicago Press (1969).
 - [2] R. P. Feynman, *Photon-hadron Interactions*, W. A. Benjamin, Inc. (1972).
 - [3] R. M. Egloff *et al.* Phys. Rev. Lett. **43**, 657660 (1979)
 - [4] J. Ballam *et al.*, Phys. Rev. D **7**, 31503177 (1973).
 - [5] H.-J. Behrend *et al.*, Nucl. Phys. **B144**, 22-60 (1978).
 - [6] D. P. Barber *et al.*, Z. Phys. C **12**, 1 (1982).
 - [7] M. Derrick *et al.* (ZEUS Collaboration) Phys. Lett. **B377** 259-272 (1996).
 - [8] H. J. Besch *et al.*, Nucl. Phys. B **70**, 257 (1974).
 - [9] J. Barth *et al.* (SAPHIR Collaboration), Eur. Phys. J. A **17**, 269 (2003).
 - [10] T. Mibe *et al.* (LEPS Collaboration) Phys. Rev. Lett. **95**, 182001 (2005)
 - [11] J. Breitweg *et al.* (ZEUS Collaboration), Eur. Phys. J. C **14**, 213-238 (2000).
 - [12] E. Anciant *et al.* (CLAS Collaboration), Phys. Rev. Lett. **85** 4682 (2000).
 - [13] D. I. Sober *et al.*, Nucl. Instrum. Methods A **440**, 263 (2000).
 - [14] M. Williams *et al.* (CLAS Collaboration), Phys. Rev. C **80**, 065208 (2009).
 - [15] T. Nakano and H. Toki, in *Proceedings of the International Workshop on Exciting Physics with New Accelerator Facilities*, SPring-8, Hyogo, 1997 (World Scientific, Singapore, 1998), p. 48.
 - [16] A. I. Titov, T.-S. H. Lee, H. Toki, and O. Streltsova Phys. Rev. C **60**, 035205 (1999).
 - [17] A. Sibirtsev, Ulf-G. Meißner, and A. W. Thomas, Phys. Rev. D **71**, 094011 (2005).
 - [18] A. Donnachie and P.V. Landshoff, Phys. Lett. B **185**, 403 (1987); Nucl. Phys. **B244**, 322 (1984); **B267**, 690 (1986).
 - [19] A. I. Titov and T.-S. H. Lee, Phys. Rev. C **67**, 065205 (2003).
 - [20] B. A. Mecking *et al.*, Nucl. Inst. Meth. A **503**, 513 (2003).
 - [21] B. Dey and C. A. Meyer, CLAS-NOTE,
 - [22] M. Williams, Ph.D. Thesis, Carnegie Mellon University, 2007, www.jlab.org/Hall-B/general/clas_thesis.html.
 - [23] M. Williams *et al.*, JINST **4**, P10003 (2009).
 - [24] W. Rarita and J. Schwinger, Phys. Rev. **60**, 61 (1941).
 - [25] M. Williams, Comput. Phys. Commun. **180**, 1847 (2009).
 - [26] Philip R. Bevington, *Data Reduction and Error Analysis for the Physical Sciences*, McGraw-Hill (1992).
 - [27] W. M. Kloet, W.-T. Chiang and F. Tabakin, Phys. Rev. C **58**, 10861097 (1998).
 - [28] M. Pichowsky, . avkli, and F. Tabakin, Phys. Rev. C **53**, 593610 (1996).
 - [29] K. Schilling, P. Seyboth, and G. Wolf, Nucl. Phys. B **15**, 397 (1970).
 - [30] F. J. Gilman, J. Pumplin, A. Schwimmer and L. Stodolsky, Phys. Lett. B **31**, 387 (1970).
 - [31] S. Ozaki, A. Hosaka, H. Nagahiro, and O. Scholten, Phys. Rev. C **80**, 035201 (2009).

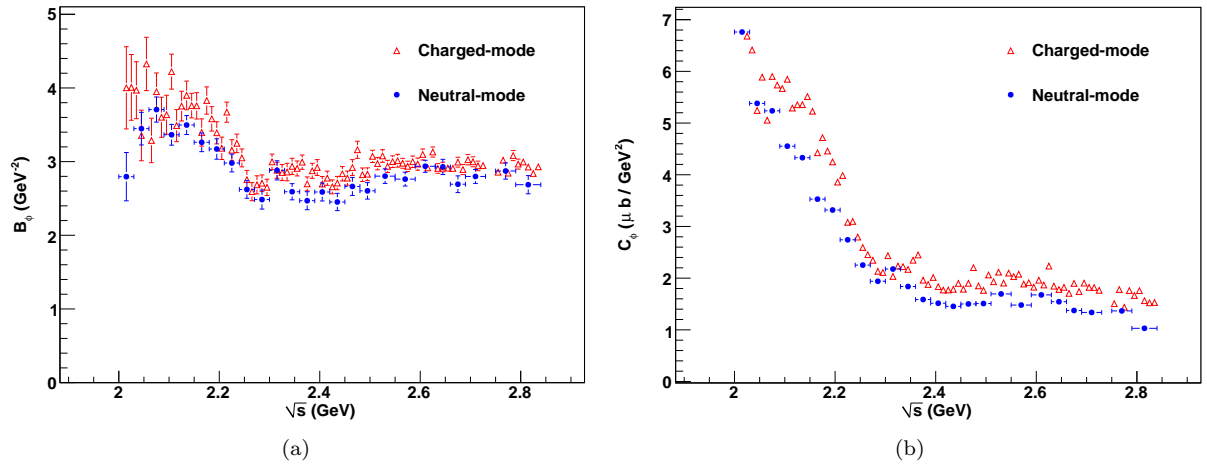


FIG. 29: (Color On-line) The variation of the parameters (a) B_ϕ and (b) C_ϕ from a fit to $d\sigma/dt$ using Eq. 31 for the charged- and neutral-modes. Only the forward-angle kinematic points satisfying $\cos\theta_{c.m.}^\phi > 0.3$ were included in the fits. See text for details.

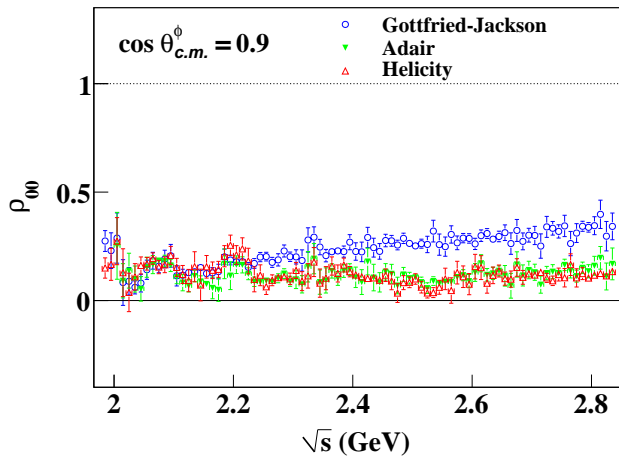


FIG. 30: (Color On-line) The ρ_{00} element is typically non-zero everywhere, in all the three reference frames. This is also true for the forward-most angular bin (diffractive region), where TCHC is strongly violated. SCHC is also violated, but to a lesser degree.

[32] J. M. Laget and R. Mendez-Galain, Nucl. Phys. **A581**, 397 (1995).

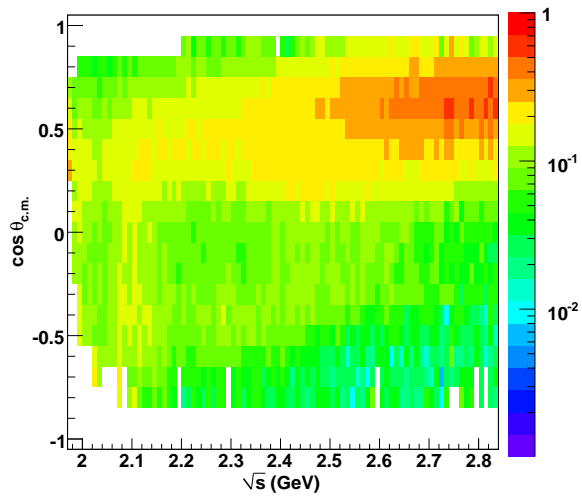


FIG. 31: (Color On-line) The ratio between the differential cross sections for ϕp and ωp photoproduction ($R_{\phi/\omega}$).